Project Title:

NeTS: Small: RUI: Bulldog Mote- Low Power Sensor Node and design Methodologies for Wireless Sensor Networks

Energy Harvesting Technologies

PD/PI Name:

Nan Wang, Principal Investigator

Woonki Na, Co-Principal Investigator: Lead Energy Harvesting Team

Recipient Organization:

California State University-Fresno Foundation

Team Members:

Maen Marji,Cheaheng Lim, and Honorio Martinez

Project/Grant Period:

10/01/2018 - 09/30/2021(no cost extension to 03/31/2021)

Reporting Period:

10/01/2020 - 09/30/2021

Signature of Submitting Official (signature shall by submitted in accordance with agency specific instructions):

ABSTRACT

This report is for the energy harvesting activities in the project, 2020~2021. During 2020~2021, a multi-source Energy harvester for low power applications have been studied explicitly. Solar and wind energy are extracted to supply a wireless sensor and charge a single-cell Li-ion battery. The maximum power point tracking (MPPT) technique implemented using DC-DC Converters for high-efficiency harvesting. Additionally, the proposed CC/CV battery charging algorithm was established based on the renewable source's maximum power availability. At the same time, the Vibration energy harvested using Piezoelectric strings is stored temporarily in a capacitor then discharged into the DC bus or directly to the load through a DC-DC converter to provide more stability to the system responses. Also, multiple control techniques have been developed, such as a linear controller (PI), a combination of linear and non-linear controllers (PI and Hysteresis switching control), and Fuzzy logic controller (FLC). Then a comparison between each controller was observed in both simulation and experimentally for MPPT and CC/CV battery charging. The multi-source energy harvester was implemented on an SMD PCB circuit prototype. Similarly, the Hysteresis switching control (HSC) was implemented as a mixed-signal design using SMD PCB.

Table of Contents

Table of Figures

List of Tables

1.9 Simulation Procedure & Results

Simulation of this project was accomplished for each renewable source separately as a stand-alone system. Hence, this ensures that each system works as expected from the designed converter and controller. The first simulation was done to the DC-DC converters without using any feedback control to guarantee that the converter works in CCM and provides the desired output voltage when a specific duty cycle is applied. Secondly, for the HSC, the PI control was designed first to achieve closed-loop compensation with a fixed reference. Third, the HSC was added to control the inductor current as an inner loop controller for a desired inductor ripple current. Finally, the INC MPPT algorithm was added to the controller to track the desired voltage and current that drive the controller to extract the maximum power from the renewable sources. Moreover, these steps were followed for every renewable source.

Figs 1.46, 1.47 shows the Simulink model for solar energy extraction using a buck-boost converter with HSC, and FLC controllers, respectively. The simulation was run for 1.25 seconds with a change of irradiance at each 0.25 second from 1000 W/m^2 to 400 W/m^2. Also, the load changes at 0.6 seconds from 10 ohms to 15 ohms. The switch control is used to direct the PWM to the required switch based on the necessary operation mode, which is the buck or the boost mode. The HSC implemented using an adder, a subtracter, two comparators, and an S-R flip flop. On the other hand, the Fuzzy was implemented using the FLC block available in Simulink. However, the output of the fuzzy is unnormalized, and compensation is done to normalize the duty cycle to be fed to the switch control.

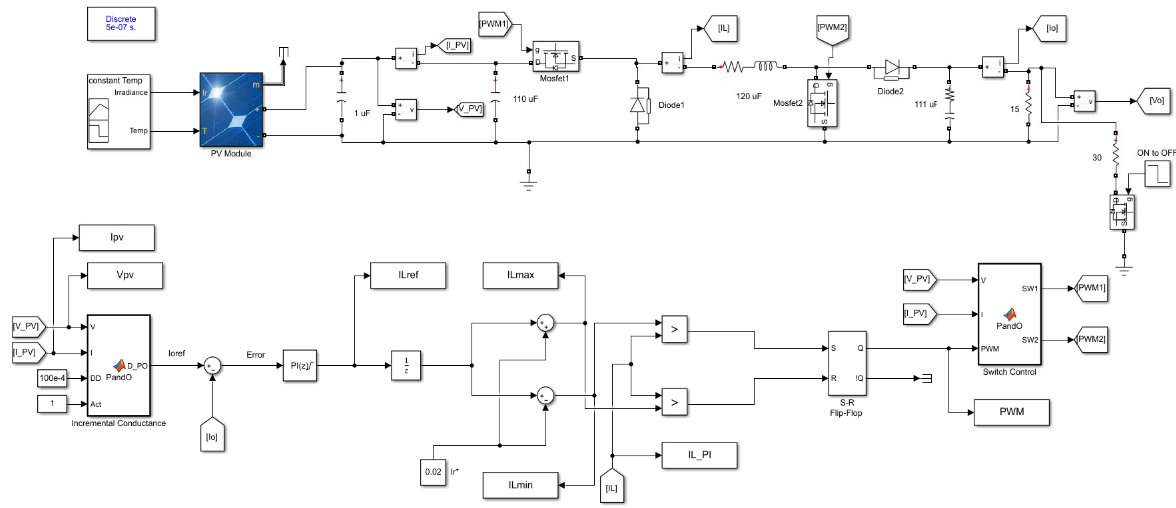

Figure 1.46: Simulink model for buck-boost converter controlled by MPPT with PI & HSC.

Figs. 1.47 & 1.48 are the solar module's simulated output power compared to the maximum power and output power at different irradiances from the DC-DC converter results by using INC MPPT with PI and HSC, respectively. The simulation results are close and achieve satisfaction in the system stability when MPPT is needed for solar energy harvesting. However, The HSC shows better responses in the worst-case scenarios, which is the highest Duty cycle where the load is low and close to the system's limitation. For the first worst-case scenario, it is clear that the PI controller becomes more oscillatory when the load changes from 10-15 compared to the HSC, where it maintains the normal operation. The second worst-case scenario is working at higher irradiance for the same critical load where the duty cycle is working at a very high percentage. The PI controller fails to achieve maximum power point tracking, while the HSC was very close to working around the MPP with minimum oscillation.

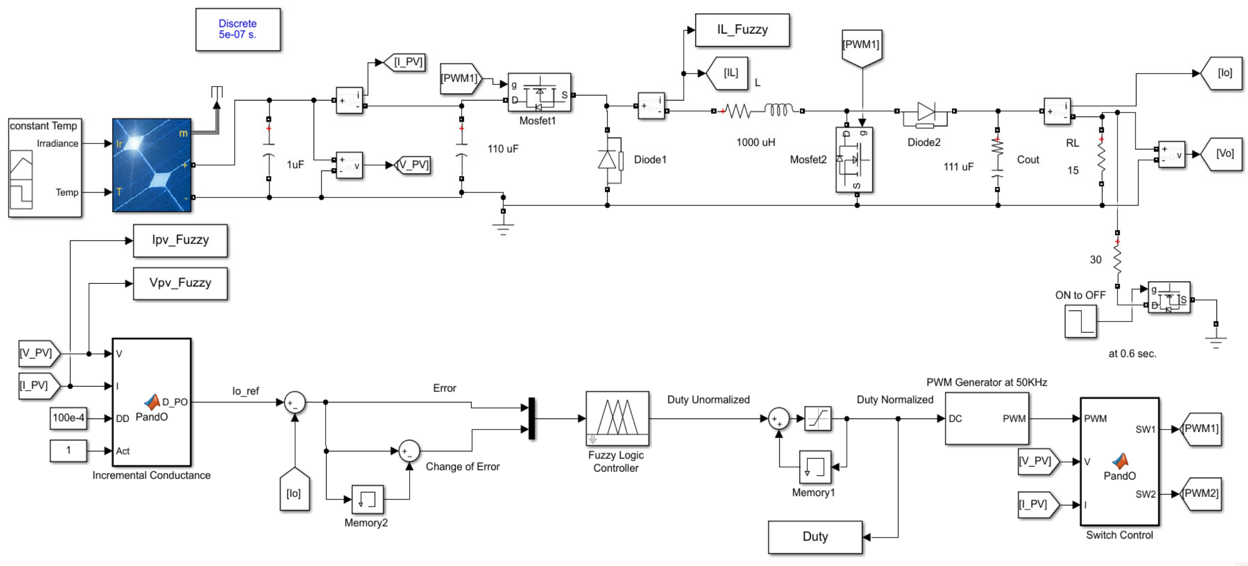

Figure 1.47: Simulink model for buck converter controlled by MPPT with FLC for solar energy harvesting.

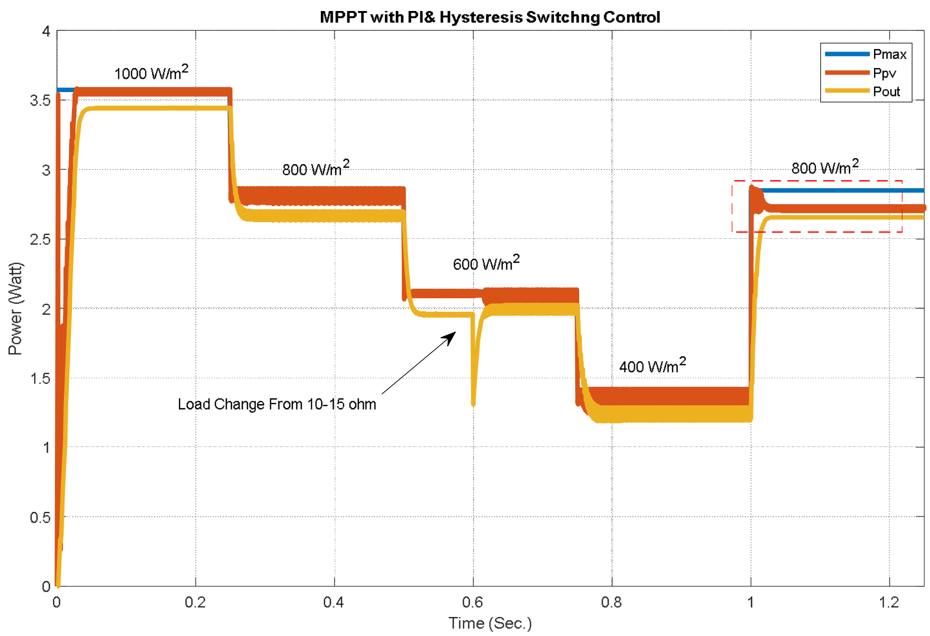

Figure 1.47: PV power and output power using only MPPT, and PI controller.

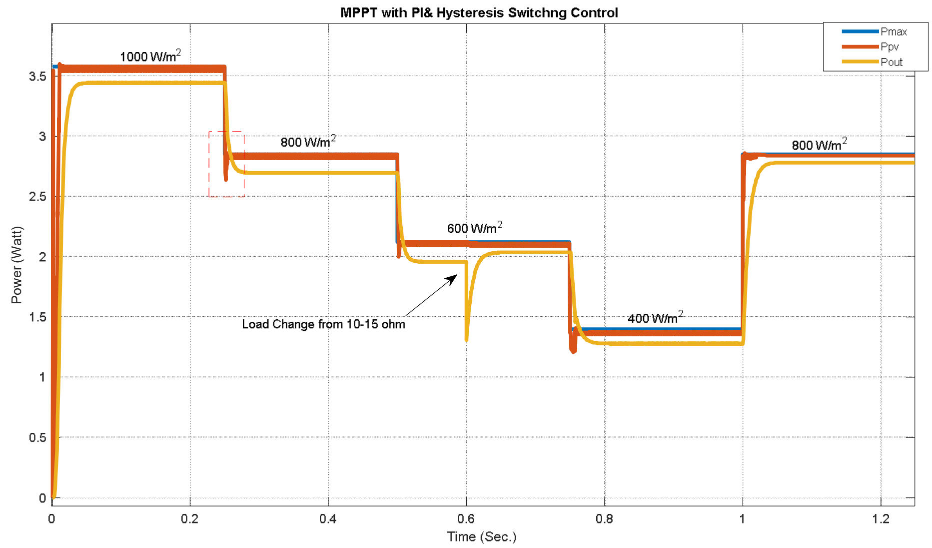

Figure 1.48: PV power and output power using MPPT, PI and HSC.

Figs. 1.49 & 1.50 are the fuzzy logic controller's simulation results, where it shows very fast responses and efficient MPP tracking for irradiance changes. However, the power oscillates more due to the fast response and the normalization process since it has a unit delay block. Thus, the operation of fuzzy logic is very efficient at higher loads, as shown in Fig.150.

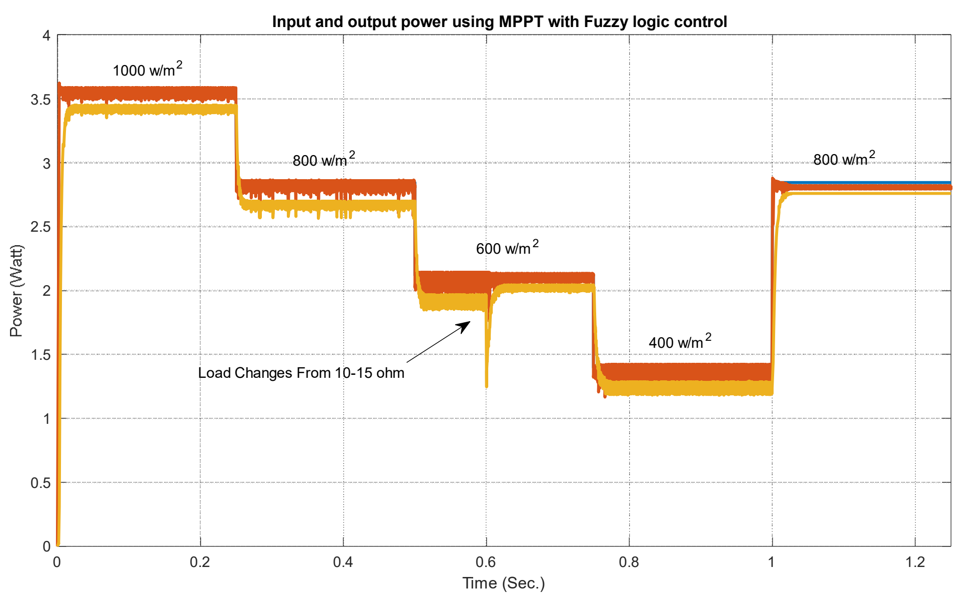

Figure 1.49: PV power and output power using MPPT with FLC and load 10-15 ohm.

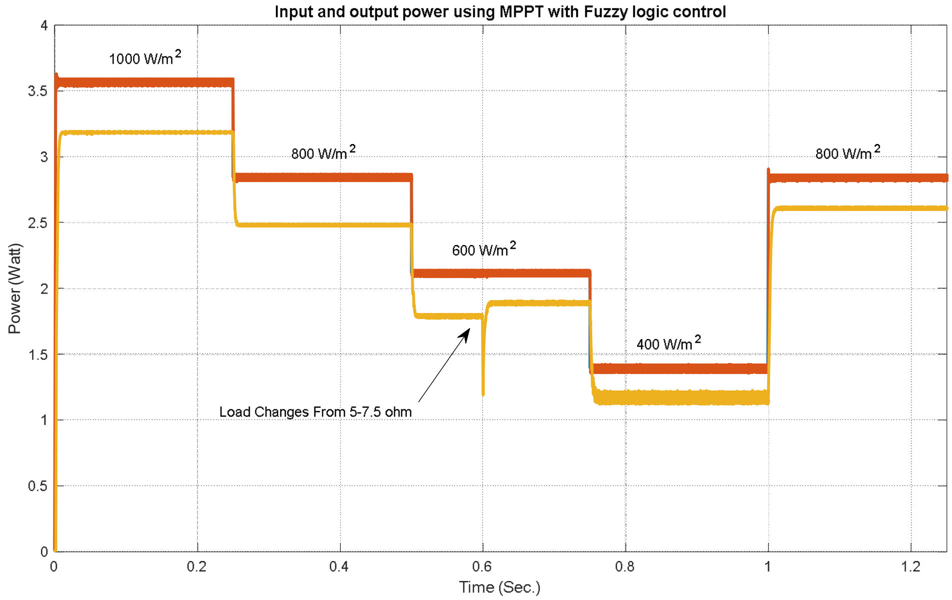

Figure 1.50: PV power and output power using MPPT with FLC and load 5-7.5 ohm.

Fig 1.51 is the inductor ripple current using PI controller where the ripple is large at lower irradiances. The PI controller oscillates more, causing such a high ripple for the inductor current, which is less efficient. Fig 1.52 represents the inductor ripple current zoomed in at 800 W/m^2 and using 10 ohms.

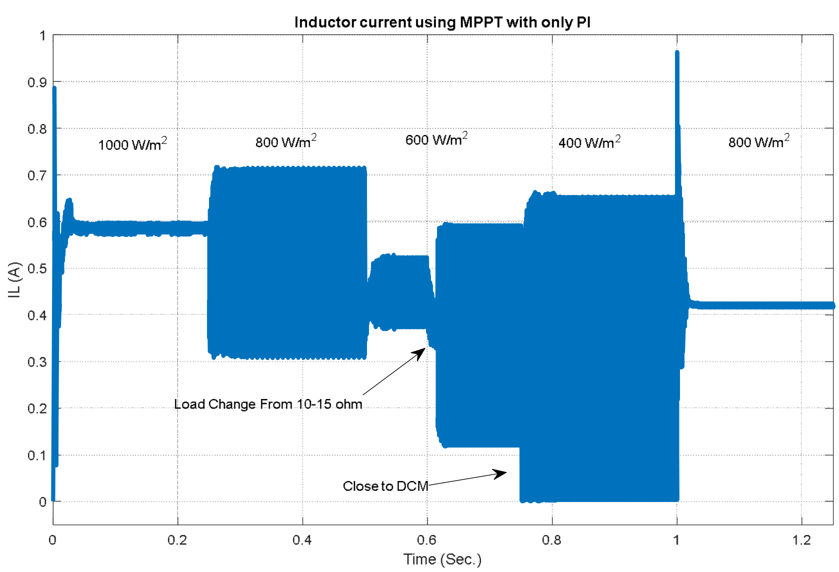

Figure 1.51: inductor current using MPPT, and PI only at different irradiances, and 10-15 ohm.

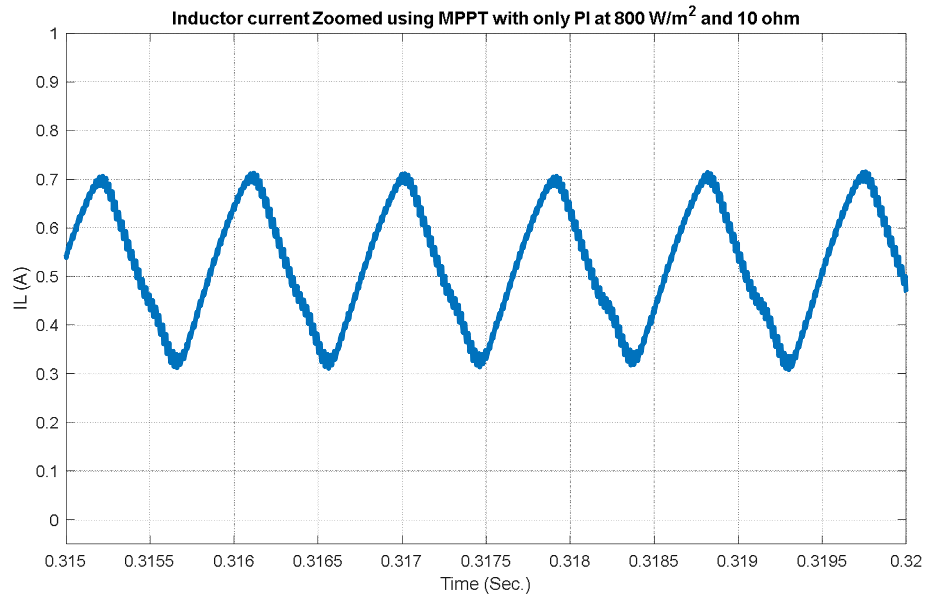

Figure 1.52: inductor current zoomed in using MPPT, and PI only at 800 W/m^2, and 10 ohms.

Figs 1.53 &1.54 represent the input/output voltages and currents at different irradiances with load changes from 10-15 ohms at 0.6 seconds using HSC and FLC, respectively. Also, Figs 1.55 shows the inductor ripple current, which seemed more controlled than using only the PI controller. This result proves that the HSC enhances the stability and robustness of the system. Fig 1.56 shows the PWM generation from the reference inductor current and the desired ripple current, which creates the boundary and then compared to the actual inductor current. The comparison will generate the PWM as discussed in the literature. Thus, Figs. 1.56 & 1.57 are the inductor current with respect to the PWM zoomed in at 1000 W/m^2 using 10 ohms and 5 ohms, respectively. At last, 1.58 & 1.59 represent the duty cycle that generates the PWM based on the inductor current comparison for different irradiances at 10 ohms and 15 ohms, respectively.

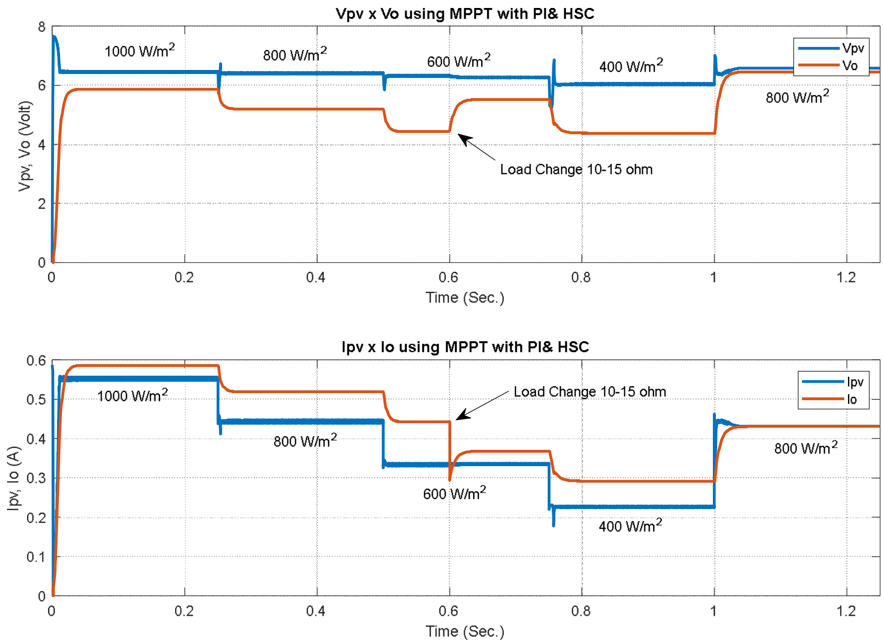

Figure 1.53: PV & output Voltage and Current using MPPT, PI and Hysteresis switching control at different irradiances.

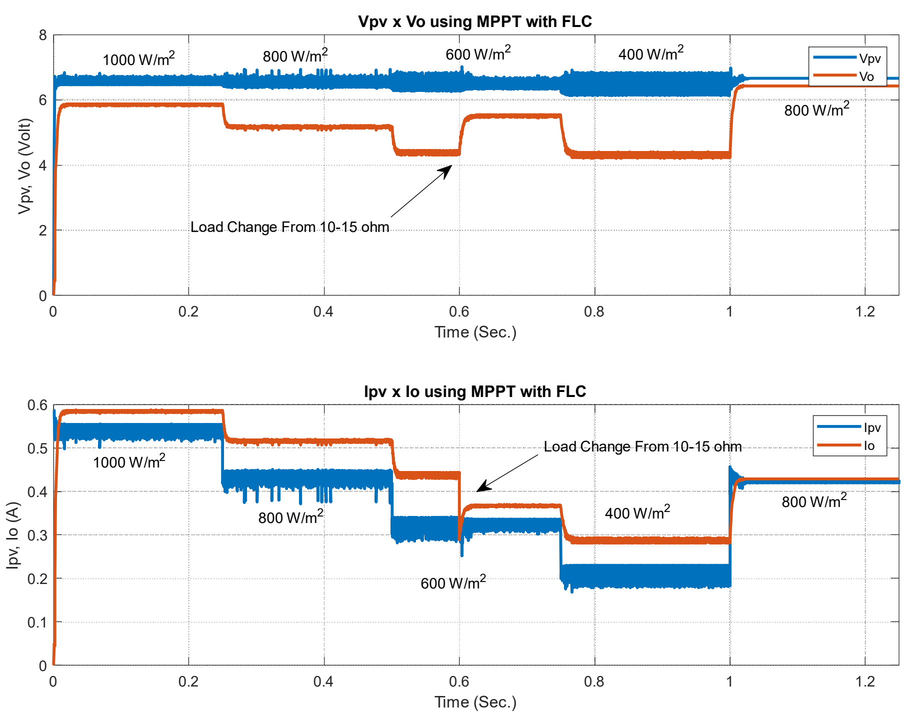

Figure 1.54: PV & output Voltage and Current using MPPT with FLC at different irradiances.

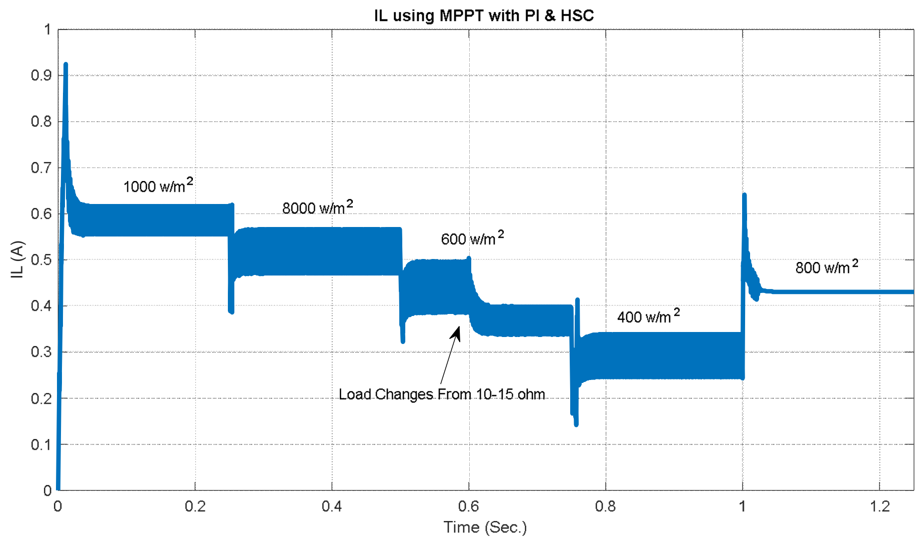

Figure 1.55: inductor current using MPPT, PI and Hysteresis switching control at different irradiances.

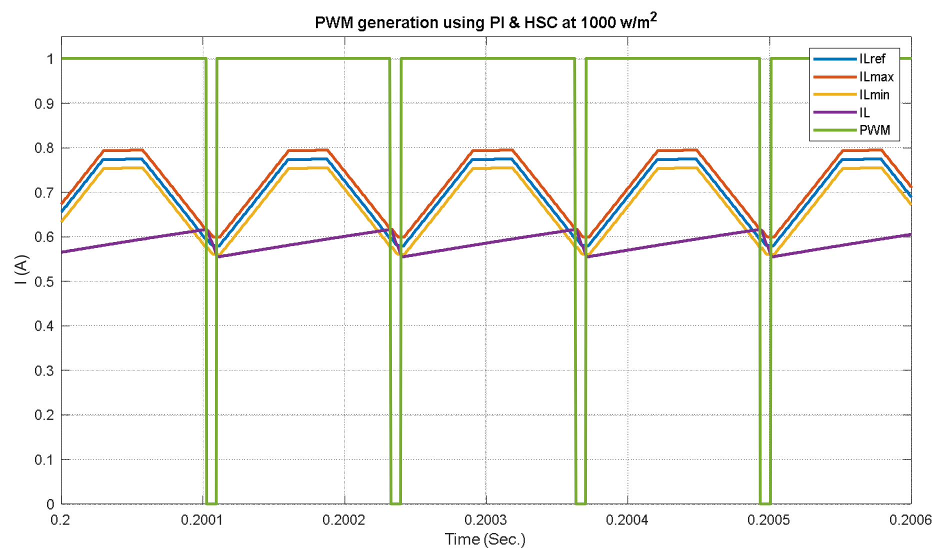

Figure 1.56: Hysteresis switching control for inductor current at 1000 W/m^2, 10 ohms, and D is 94.5%.

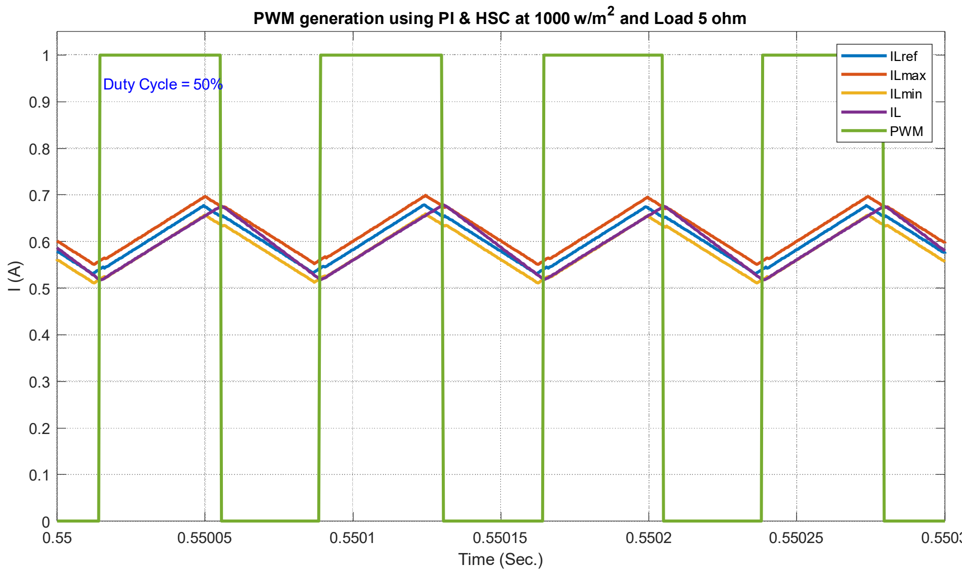

Figure 1.57: Hysteresis switching control for inductor current at 1000 W/m^2, 5 ohms, and D is 55%.

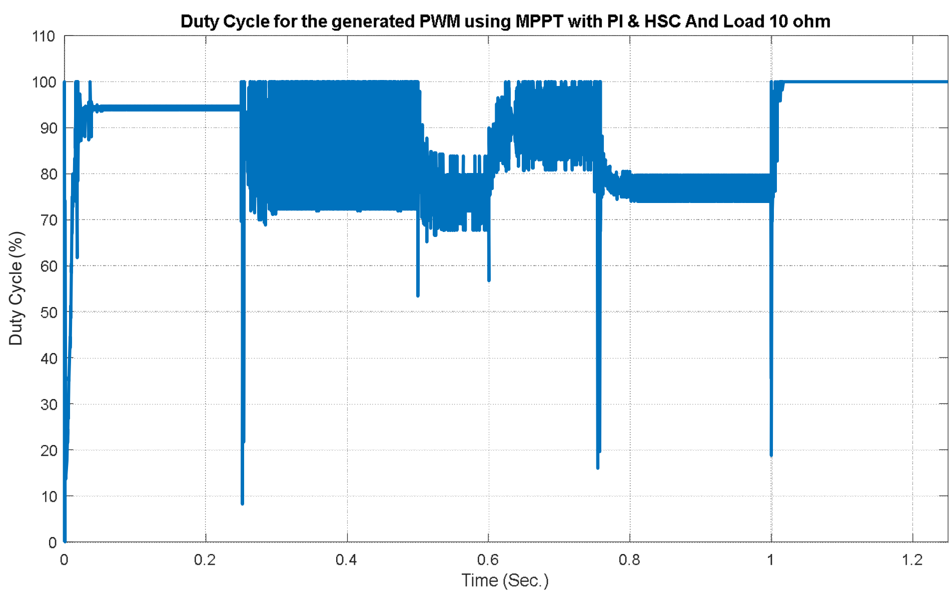

Figure 1.58: Duty cycle using MPPT, PI and Hysteresis switching control at different irradiances using 10-15ohm, 15 ohms at 0.6 sec.

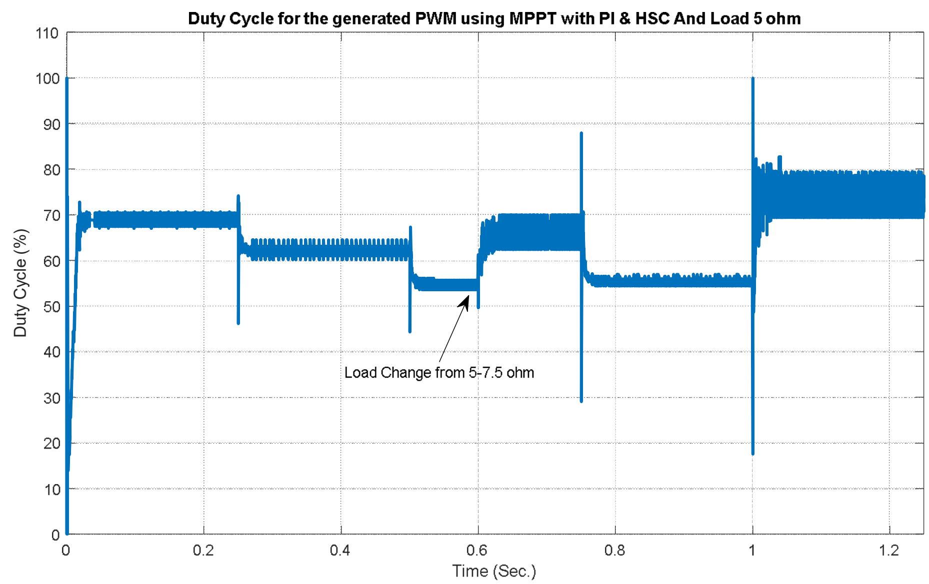

Figure 1.59: Duty cycle using MPPT, PI and Hysteresis switching control at different irradiances using 5-7.5-ohm, 7.5 ohm at 0.6 sec.

For the simulation of wind energy harvesting (Fig. 1.60), the wind turbine block diagram's output mechanical torque was fed into the PMDC generator. Thus, the output power will depend directly on the wind speed. Fig. 1.61 shows the motor shaft speed and the induced electrical torque with respect to changing wind speed. Also, the load changes at 4 seconds from 10-7.5 ohm.

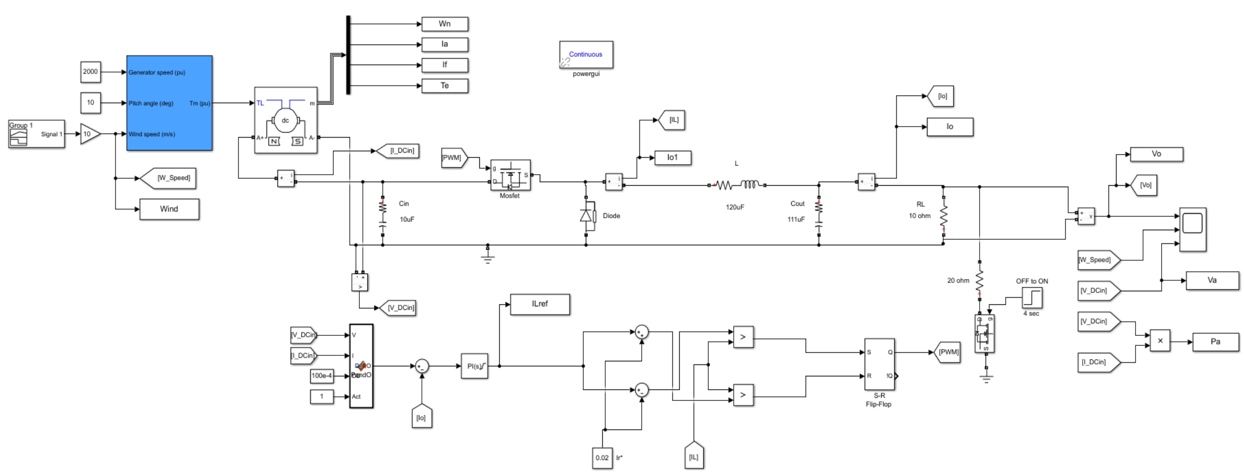

Figure 1.60: Simulink model for buck converter controlled by MPPT with PI & HSC for wind energy harvesting

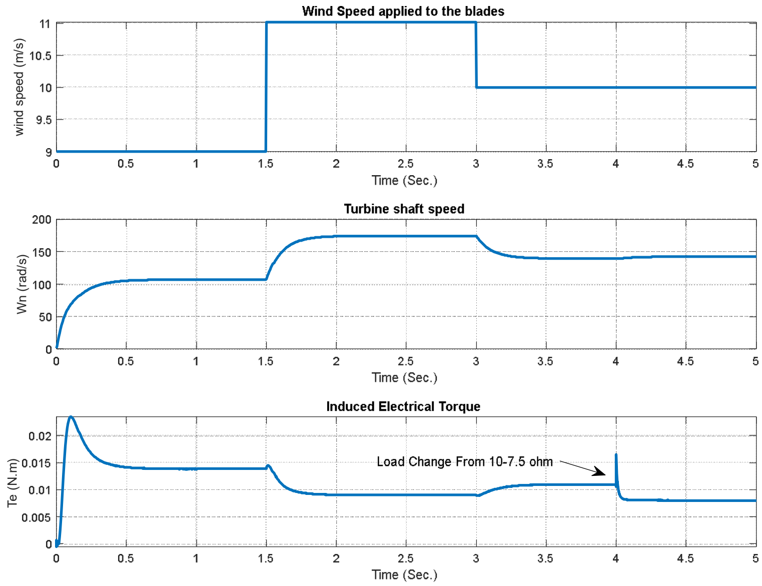

Figure 1.61: Turbine speed and induced electrical voltage at different wind speed.

Fig. 1.62 shows the input and the output voltage and current with different wind speed where the buck converter controlled using constant current. The output current is set to be 0.35A (red), where the duty cycle changed to keep the output current at that set point, as shown in Fig. 1.63. In addition, Fig. 1.63 show the inductor ripple current at different irradiances.

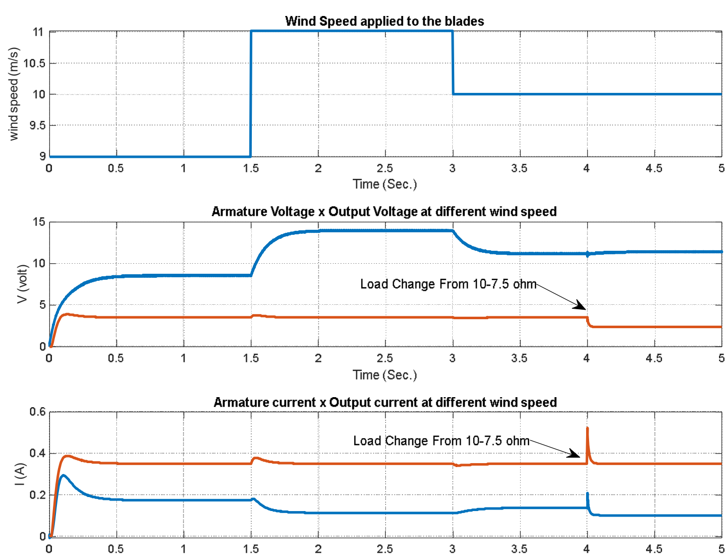

Figure 1.62: Va, Vo, Ia, and Io at different wind speed, and load changing from 10-7.5 ohm.

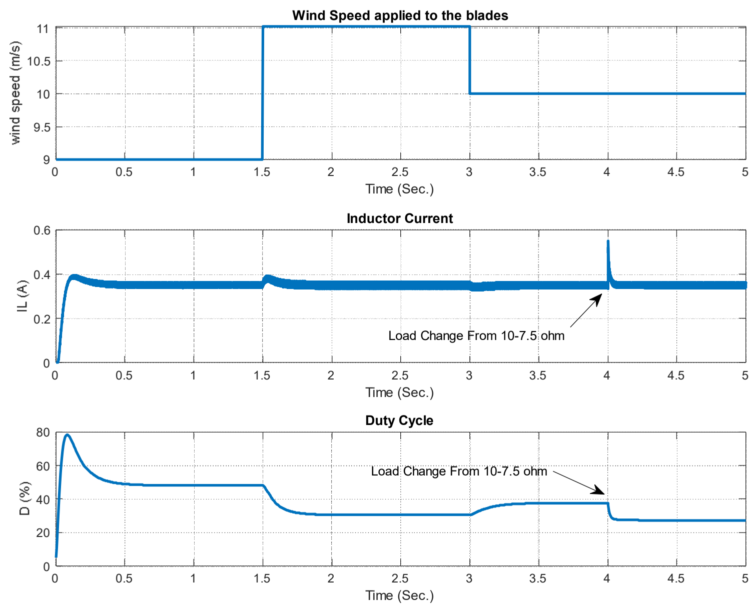

Figure 1.63: Inductor current, and Duty cycle at different wind speed.

Finally, the vibration energy harvesting simulation was done using multiple strings connected in parallel to increase the total output current, as shown in Fig. 1.64. After that, a rectifier was used to convert the AC power into DC power then store it temporarily in the Coupling capacitor. Then the power is released to the system using buck converter with PI controller to feed the load with 3 volts, or the bus with a voltage around 4.2 V. Fig 1.65 shows the effect of feeding the stored energy into the bus when one of the renewable sources disconnected.

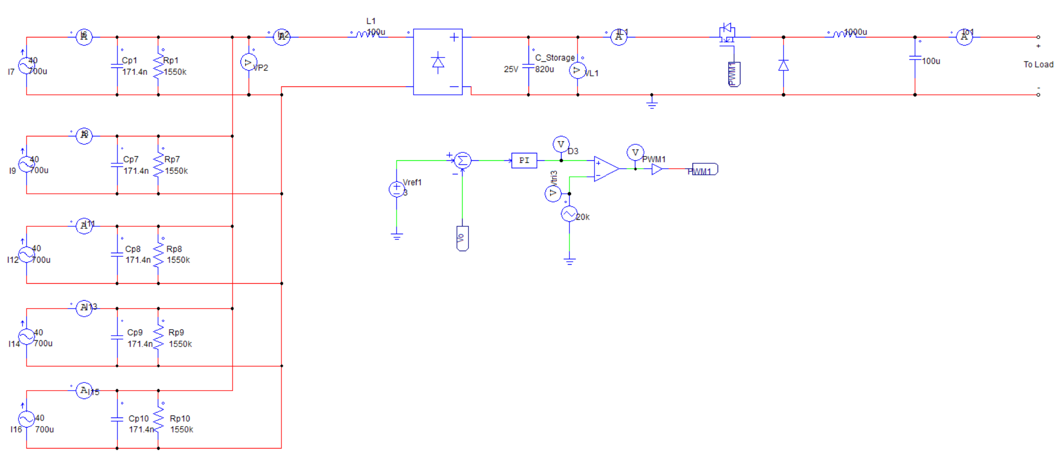

Figure 1.64: Simulation model for multistring Piezoelectric harvester.

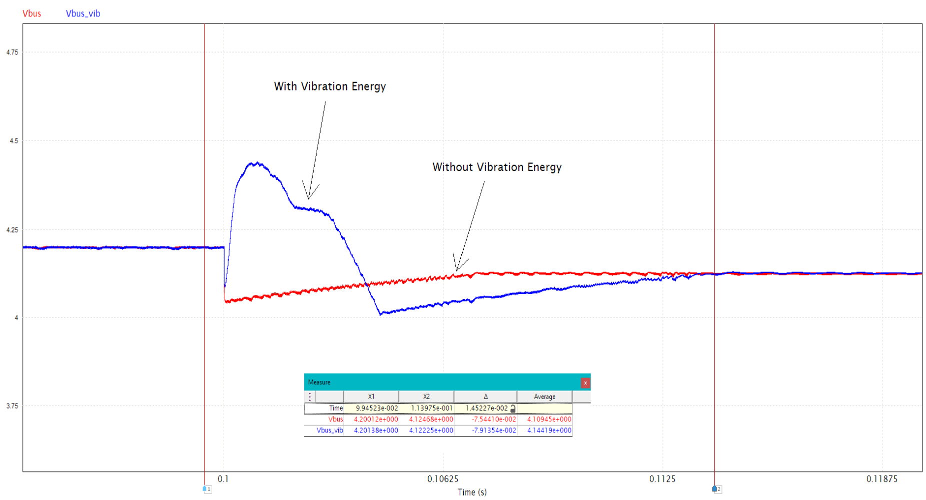

Figure 1.65: piezoelectric generation effect at the bus voltage when wind energy disconnected from the system.

1.10 Hardware Implementation

The implementation of the project was accomplished in multiple steps. The first step was designing the hardware for both the DC-DC converters and the controller. The second step was implementing the control algorithms on a microcontroller to produce the PWM signal for each switch in the multi-source renewable energy harvester. The last step was to test the hardware and software by collecting data to match the simulation as close as possible.

The PCB schematic for the whole controller is shown in Fig. 1.66. The voltage divider method was used to sense the input, bus, load, and battery voltage. The sensed value was inserted into a non-inverted buffer to isolate the voltage divider from the equivalent circuit of the Analog to digital converter (ADC) on the microcontroller. The values of R1 and R2 were chosen based on the maximum input voltage and the rating of the ADC; this will shift the voltage from high values to the rating of the ADC input pin voltage. Fig. 1.67 shows the voltage sensor circuit where a 0.1 uF capacitor is used to eliminate the noise for accurate sensing. The buffer op-amp has a medium slew rate with rail-rail output. Table A.1 in Appx. A show all the component selection used for the multi-source energy harvester.

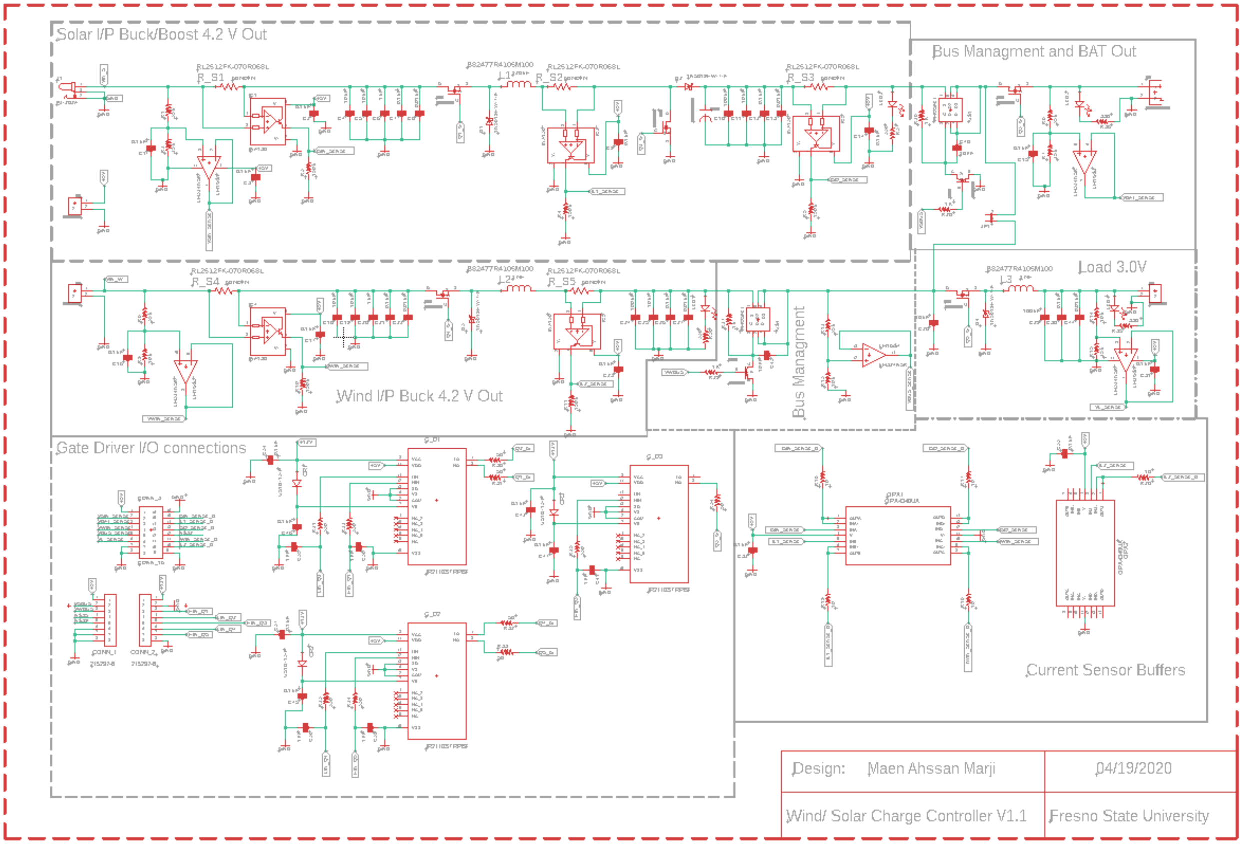

Figure 1.66: Multi-source energy harvester PCB schematic.

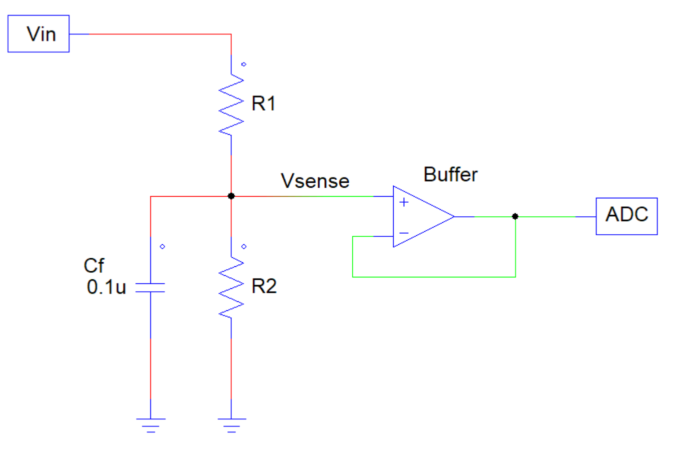

Figure 1.67: Voltage sense circuit.

For the current sensing circuit, a fast-high side current monitor with a fast slew rate Op-Amp was selected. Fig 1.68 shows the current sensing circuit where the shunt resistor is small to reduce the losses. The sensing will depend on the voltage difference across the shunt resistor, which is related to the current passing that resistor. Also, the resistor on the output will determine the sensor's gain, and it can be calculated based on Eq. 1.52 [34]. In addition, the current sensor used to measure the inductor current must be located after the inductor since the voltage before the inductor varies between 0-Vin. This voltage will make the current sensor malfunction and read a faulty value. In contrast, the voltage is steady after the inductor and make the reading accurate and stable.

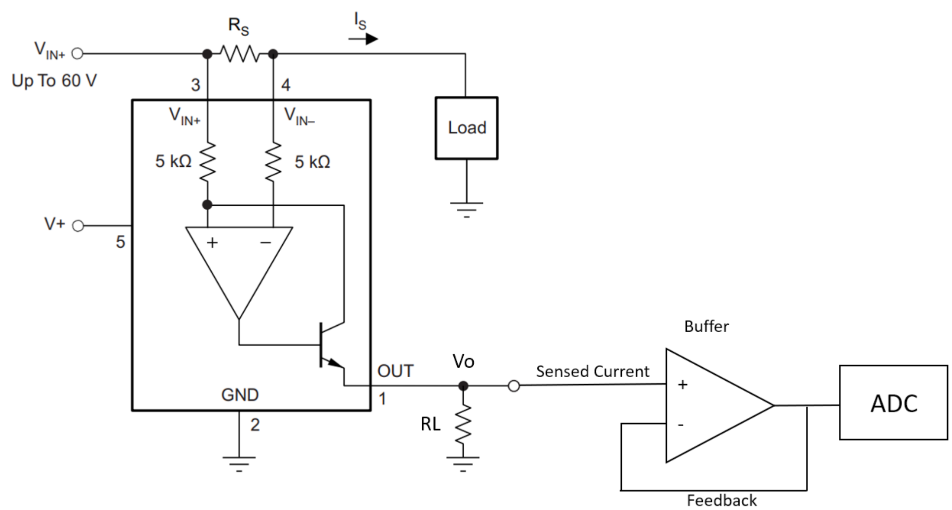

Figure 1.68: High-side current sensing circuit [34].

$$V_o = \frac{I_s R_s R_L}{5k\Omega} \quad (1.52)$$

The switch in the DC-DC converter was chosen to be a MOSFET due to its fast switching speed and low power dissipation. However, the PWM signal coming from the controller is either 3.3 V or 5 V, which is not enough to turn the switch on. Thus, a gate driver was used to shift the PWM signal from 3.3 or 5V to 10-20 V based on the supply voltage. The gate driver circuit is shown in Fig. 1.69, where a 10nF and 330 ohms was used at the input to reduce the spikes and ringing that appears on the generated PWM.

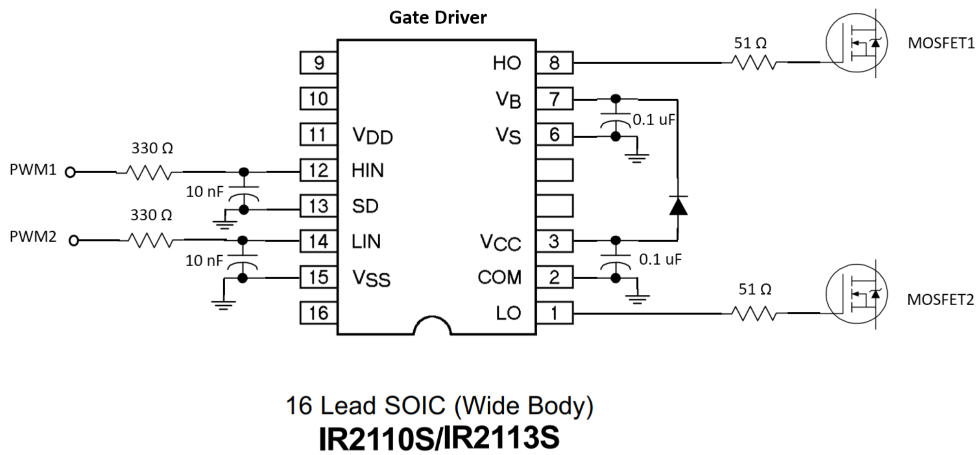

Figure 1.69: Gate driver circuit [35].

The circuit was implemented using four layers of SMD PCB design. The layers of the board are shown in Fig. 1.70. the top and the bottom layers are utilized by the component, while layer two is ground, and layer three is 5-12 supply voltage. Also, the DRC rules in Table 1.8 were strictly followed. The board after soldering the component is shown in Fig 1.71.

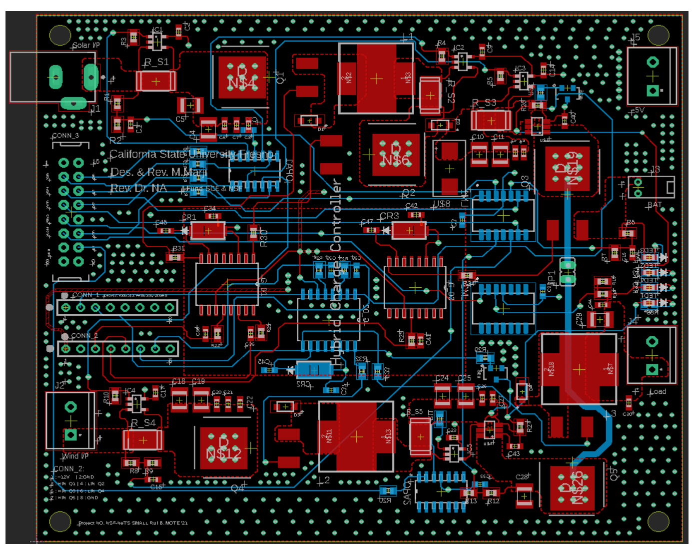

Figure 1.70 The PCB layers of the Multi-source energy harvester.

TABLE 1.8: DRC RULES USED IN THE PCB DESIGN.

DRC	Value	
Layers	Copper	0.035 mm
	Core	1.5 mm
	Copper	0.035 mm
clearance	Wire	8 mil
	Pad	8 mil
	Via	12 mil
Distance	Copper/Dim.	20 mil
	Drill/Hole	12 mil
Thermal Isolation	10 mil	
Size	6 mil	
Board Dimension	116 x 96 mm	

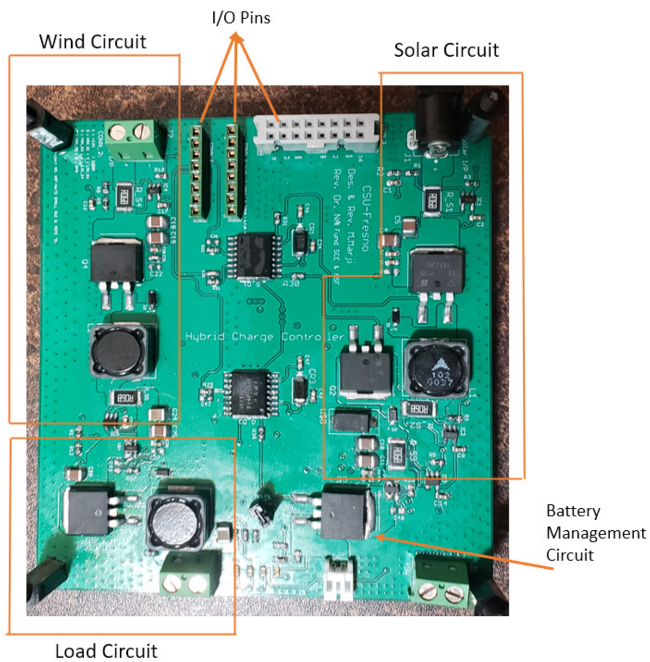

Figure 1.71: SMD PCB board with the component soldered.

The HSC was implemented using analog and digital mixed circuit design, as shown in the Spice model in figure 1.72. IL_max and IL_min come as a high PWM signal due to the absence of DAC in the chosen microcontroller. Therefore, the DAC was built using a first-order RC active filter with a gain of one and a time constant equal to 0.5 milliseconds to generate the PWM that drives the converter switch after comparing the actual inductor current. For the RC filter design, Eq. 1.53 was used with a cutoff frequency around 320 Hz to get the DC value from the high-frequency HRPWM signal coming from the DSP PWM pin. The PCB schematic and the SMD printed board are shown in Figs. 1.73 & 1.74, respectively. Table A.2 in Appx. A show all the component selection used for the HSC analog implementation.

$$f_c = \frac{1}{2\pi RC} \tag{1.53}$$

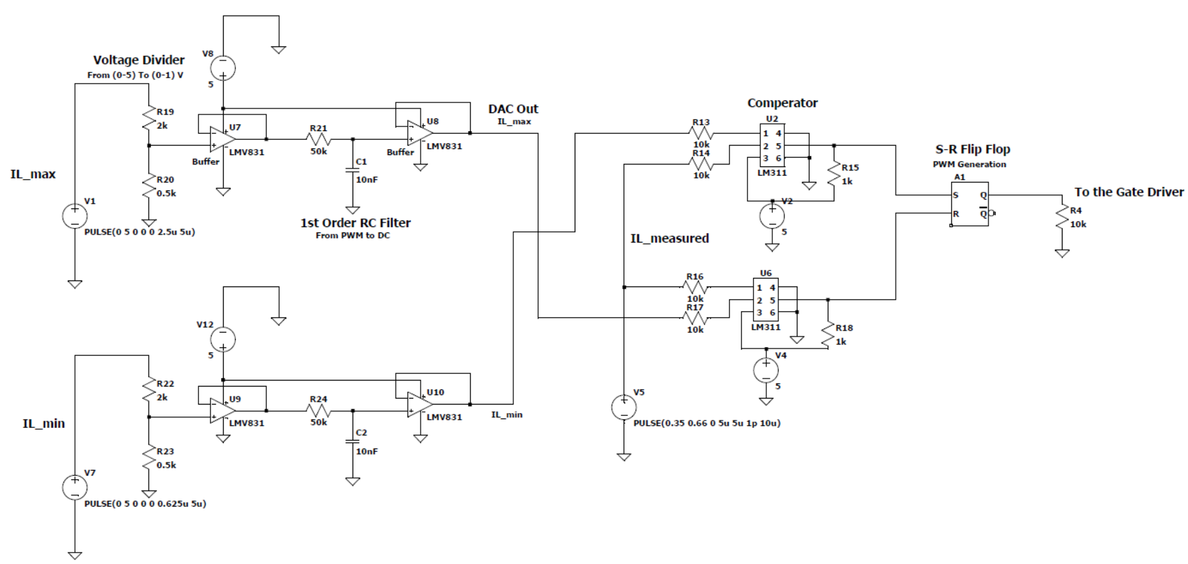

Figure 1.72: Spice Model of the HSC.

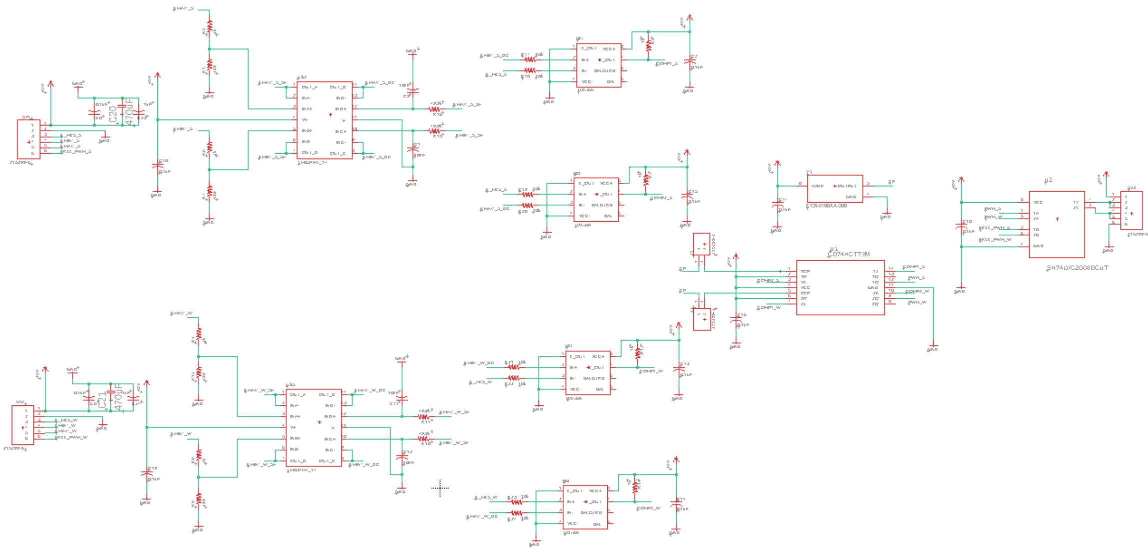

Figure 1.72: HSC mixed signal implementation PCB schematic.

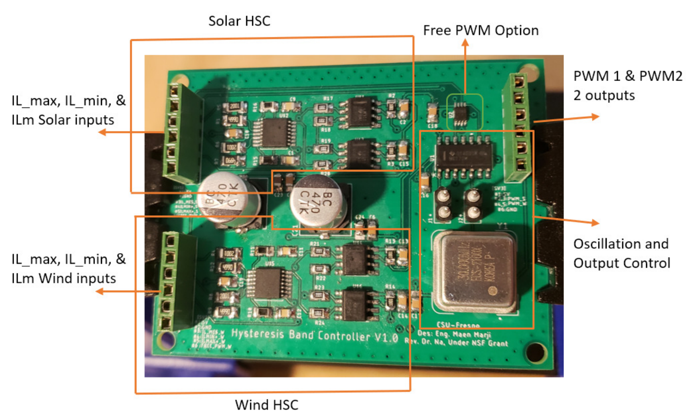

Figure 1.73: SMD PCB of the HSC.

The minimum and maximum inductor current are calculated based on adding and subtracting the reference inductor current, which is the PI controller output. The PI was implemented as software in the microcontroller TMSF28335 designed by Texas Instruments. This microcontroller can interface with MATLAB, and it allows reprogramming during run time. The flexibility provided in the microcontroller allows monitoring and tuning the control algorithms instantaneously. The software is a built-in Simulink model, and then the code is generated and linked to the microcontroller. The microcontroller is a built-in control card developed by TI that inserted into a development board developed by Power Simulation Inc [36].

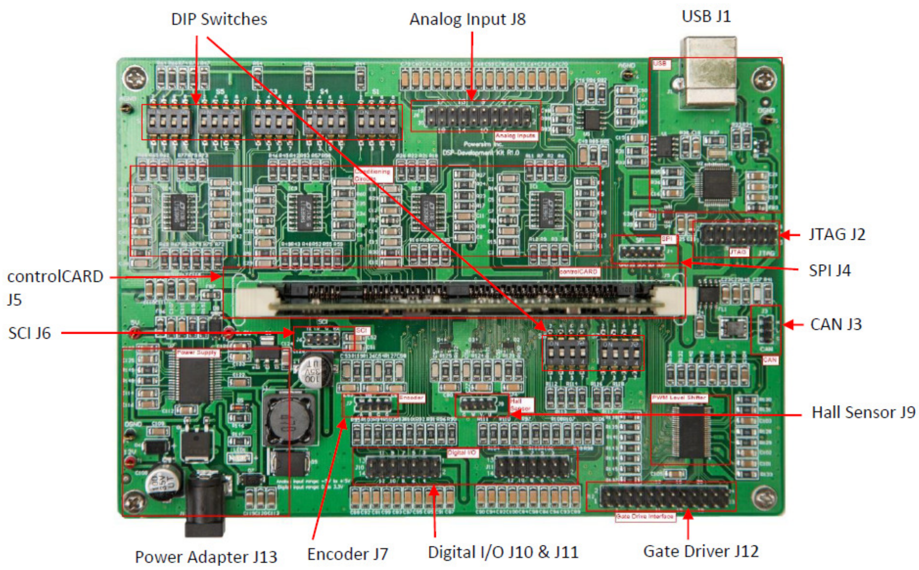

Figure 1.74: DSP control board diagram [36].

The HSC embedded Simulink model is shown in Fig. 1.75, where IL_ref is calculated using discrete-time PI controller with unit delay on the output. After that, the reference value is added and subtracted from a desired inductor current ripple value Ir*. Also, Monitoring the inputs, outputs, and control signals during runtime are done using the Simulink scopes. Furthermore, the overall embedded Simulink model for FLC, including Solar, Wind, and battery charging algorithm, is shown in Figs. 1.76.

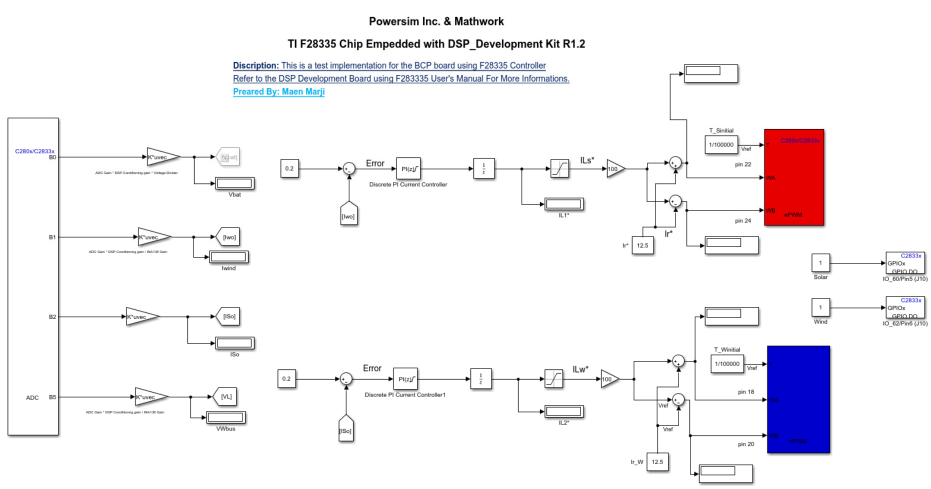

Figure 1.75: Embedded Simulink model for the renewable energy harvester using HSC.

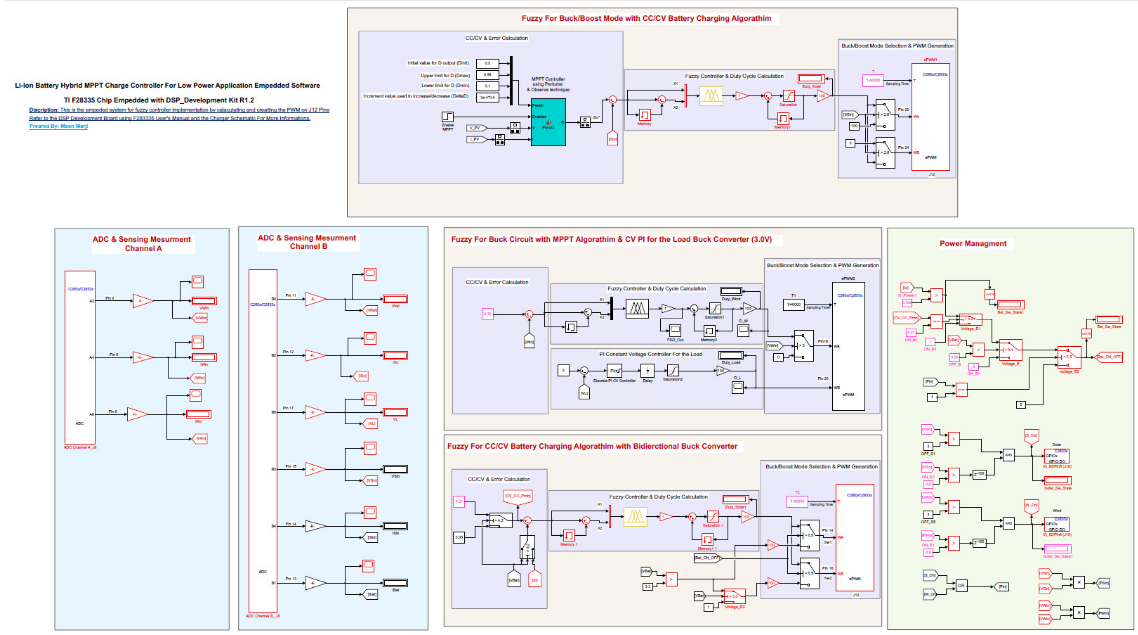

Figure 1.76: Embedded Simulink model for the renewable energy harvester using FLC.

1.11 Experimental Results

The experimental results were collected to match the irradiance variation that has been done in the simulation. Thus, Figs. 1.77-1.79 shows the comparison between the extracted power from the solar module at different irradiances using PI, HSC, and FLC, respectively. However, the overall efficiency seemed to be less than expected compared to the simulation results. This happens when the simulation model does not include all the nonlinearities in the system. Tables 1.9 & 1.8 show all the experimental results for response time and expected MPP.

Some of the experimental results were collected using the scope of the Simulink model. The ADC sampling frequency was selected to be 200 Hz. This slow sampling frequency was chosen because the Simulink scope's slow speed prevents capturing all the collected data captured at a higher sampling frequency.

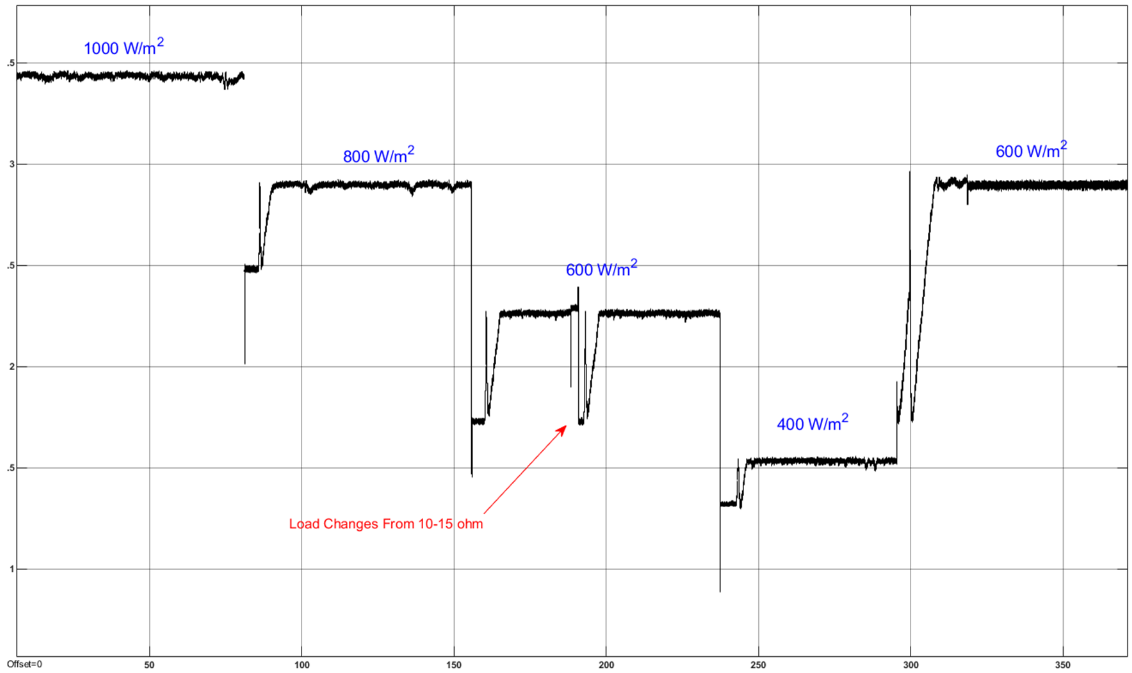

Figure 1.77: Solar Energy Harvesting using buck with INC MPPT, and PI at different irradiances.

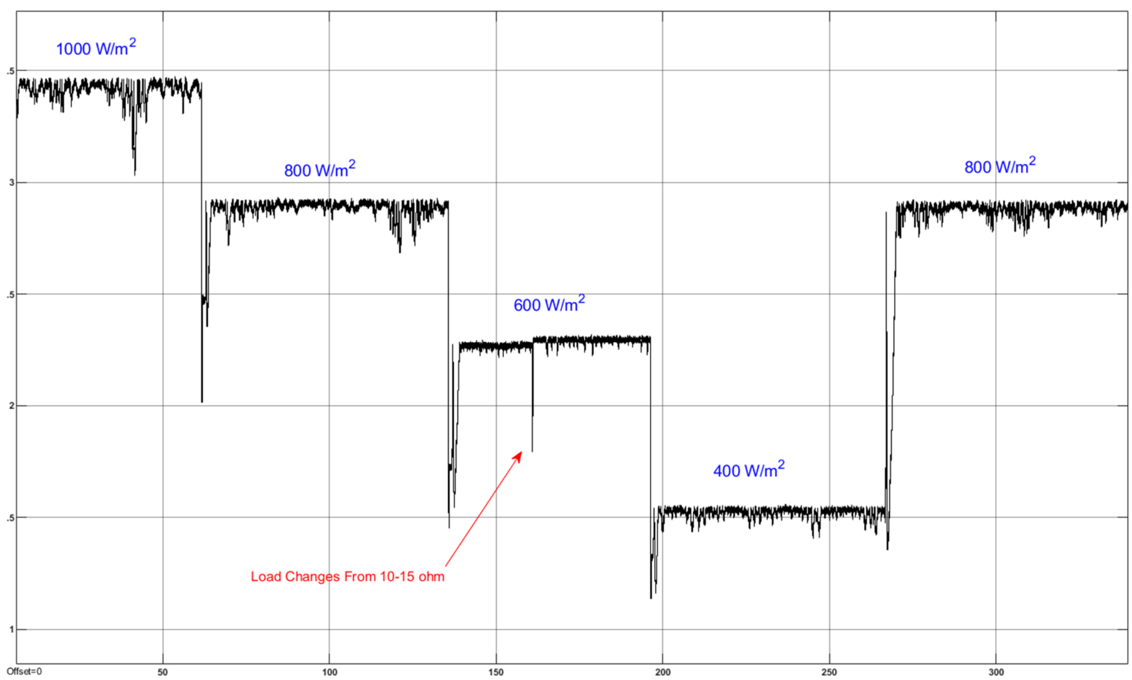

Figure 1.78: Solar Energy Harvesting using buck with INC MPPT, PI & HSC at different irradiances.

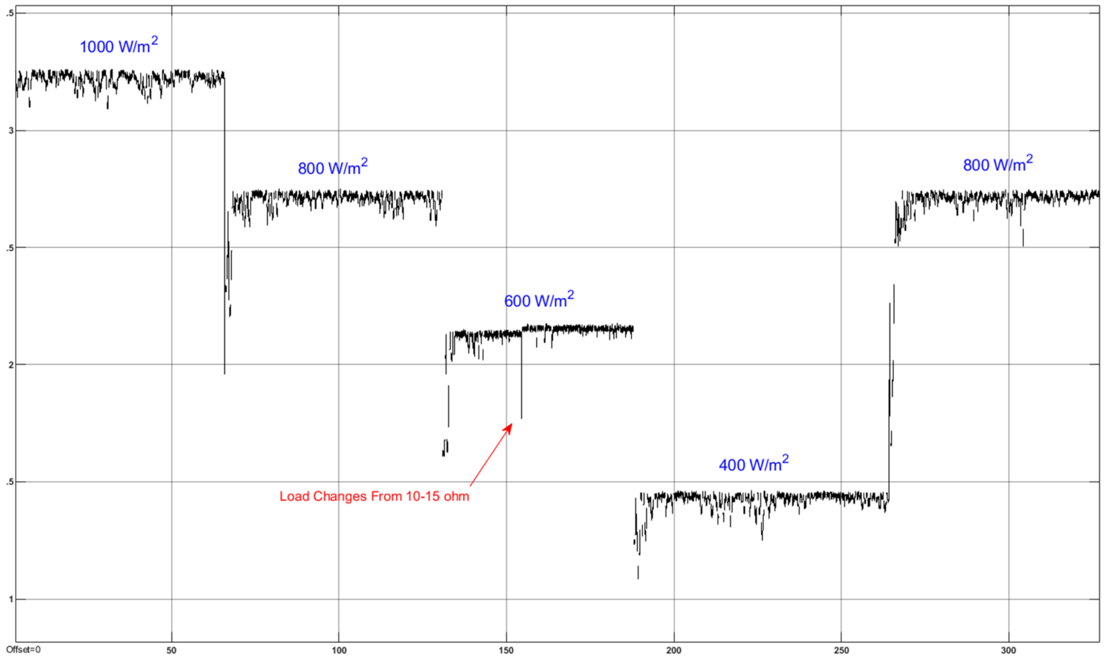

Figure 1.79: Solar Energy Harvesting using buck with INC MPPT and FLC at different irradiances.

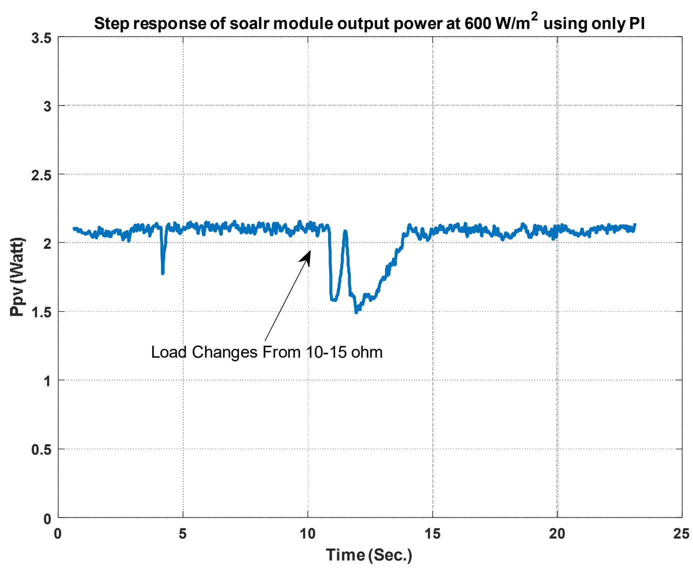

Figure 1.80: Zoomed in at 600 W/m^2 when load change from 10-15 ohm using only PI (captured using oscilloscope)

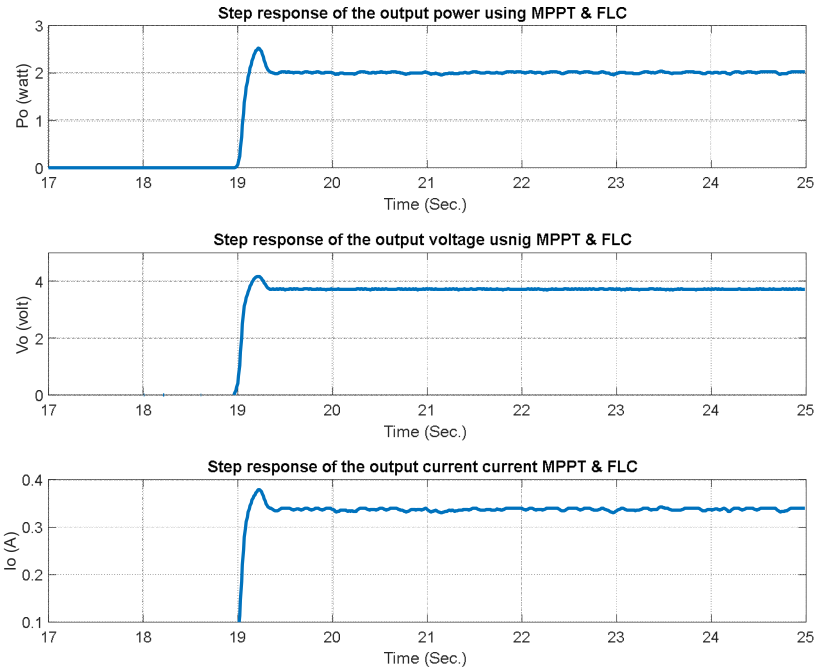

Figure 1.81: Step responses of the output power, voltage, and current from 0 to 600 W/m^2.

TABLE 1.9: EXPERIMENTAL RESULTS ANALYSIS FOR MPPT USING DIFFERENT CONTROLLERS.

Analysis Type/ Controller Type		FLC				HSC & PI				PI			
		1-0.8	**0.8-0.6**	**0.6-0.4**	**0.4-0.8**	**1-0.8**	**0.8-0.6**	**0.6-0.4**	**0.4-0.8**	**1-0.8**	**0.8-0.6**	**0.6-0.4**	**0.4-0.8**
Res. Time (Sec.)	**Exp.**	**1.9**	**2.1**	**2.3**	**2.7**	**3**	**3.1**	**3.1**	**3.6**	**5**	**5.5**	**5.3**	**6.8**
	Act.	2.09	2.3	3	2.3	4.19	3.2	4.4	5.4	10.67	9.4	8.8	12.7
MPP (Watt)	**Exp**	**3.55**	**2.95**	**2.3**	**1.55**	**3.55**	**2.95**	**2.3**	**1.55**	**3.55**	**2.95**	**2.3**	**1.55**
	Act.	3.34	2.82	2.21	1.49	3.44	2.93	2.3	1.54	3.4	2.89	2.27	1.53

TABLE 1.10: EXPERIMENTAL RESULTS ANALYSIS FOR LOAD CHANGING AT 600 W/M^2

Analysis Type/ Controller Type		FLC	HSC & PI	PI
		10-15 ohm	**10-15 ohm**	**10-15 ohm**
Res. Time (Sec.)	**Exp.**	**0.4**	**1.1**	**2**
	Act.	0.5	1.3	6.5
MPP (Watt)	**Exp**	**2.28-2.28**	**2.31-2.31**	**2.3-2.3**
	Act.	2.21-2.25	2.3-2.307	2.27-2.9

Figs 1.82 & 1.83 are the charging profile of the 350 mAh li-ion battery. The battery start charging at 0.35 A using constant current mode until the battery voltage reaches 4.2 V. After that, the battery continues charging at 4.2 using constant voltage until the current reaches 0.1C of the battery rated capacity. This follows the CC/CV voltage algorithm discussed in Sec.1.5.

The first controller used to charge the battery was HSC, where Fig. 1.84 shows the inductor ripple current with the boundary to create the PWM signal. The HSC charges the battery to SOC equals 85%. The poor performance of HSC in battery charging applications refers to the distortion in the inductor current at high SOC, which makes the comparison fail. Thus, the system becomes unstable at a small charging current, and it makes the controller's output equal to zero. The inductor ripple current shown in Fig. 1.85 is captured at the start of charging, which has a duty cycle of 60%, while Fig. 1.86 shows the inductor ripple current at 100 mA charging current with 45% duty cycle. In contrast, FLC shows better performance in charging the battery. Figs. 1.87 & 1.88 show that the inductor ripple is less by half compared to HSC and the controller was able to charge the battery efficiently until SOC above 95%. Finally, Fig. 1.89 shows the step response of HSC when a load is connected in parallel with the battery, causing a sudden increase in the current. However, the controller adjusts the duty cycle and frequency to keep the error close to zero as much as possible.

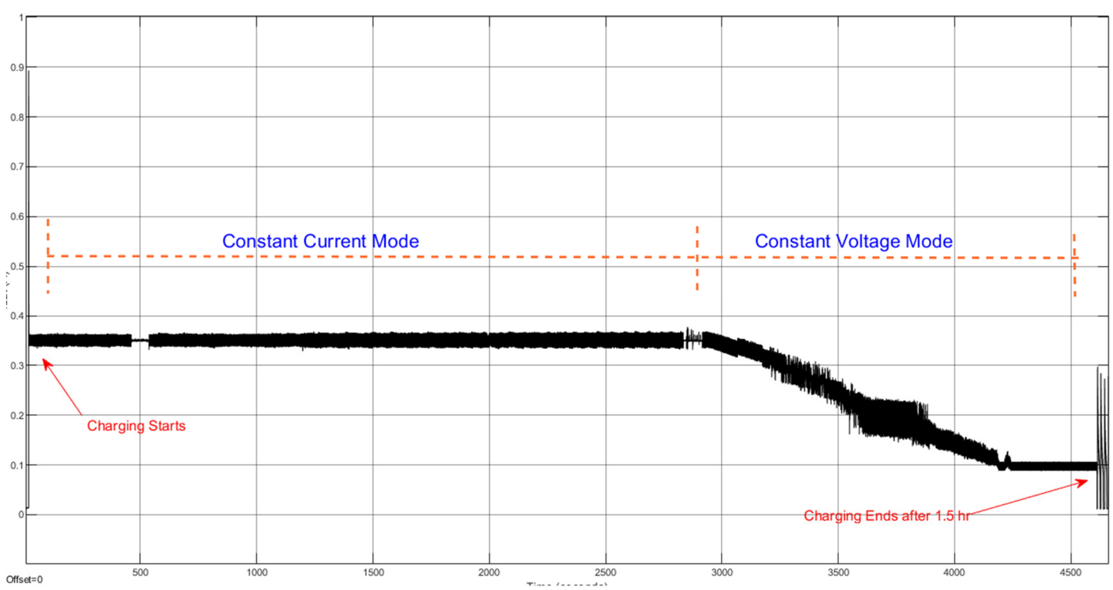

Figure 1.82: The battery charging current profile using CC/CV algorithm & HSC.

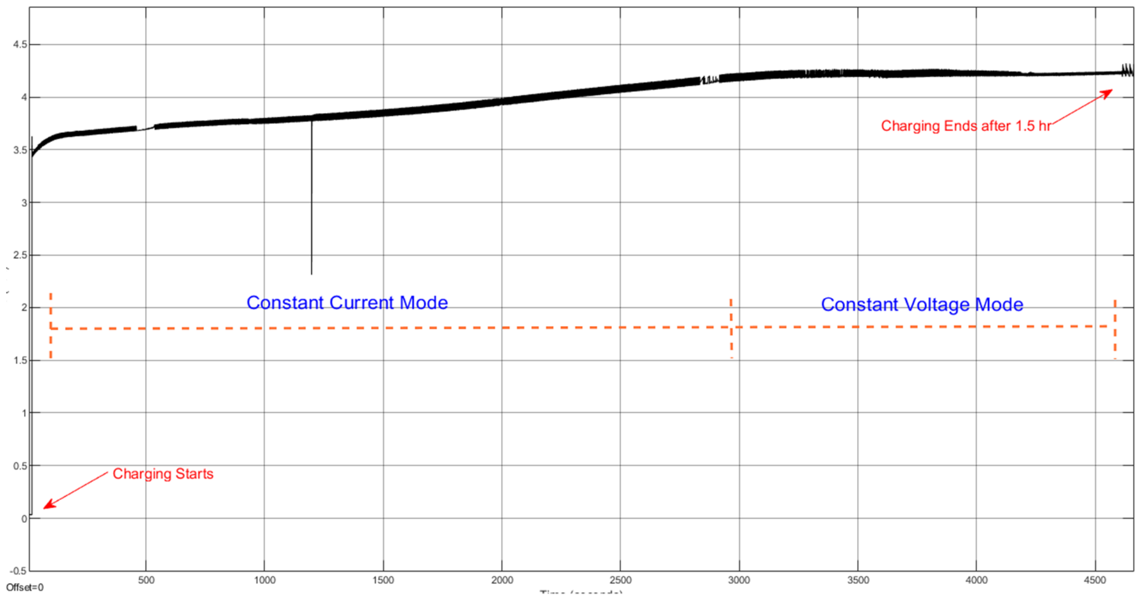

Figure 1.83: The battery charging voltage profile using CC/CV algorithm & HSC.

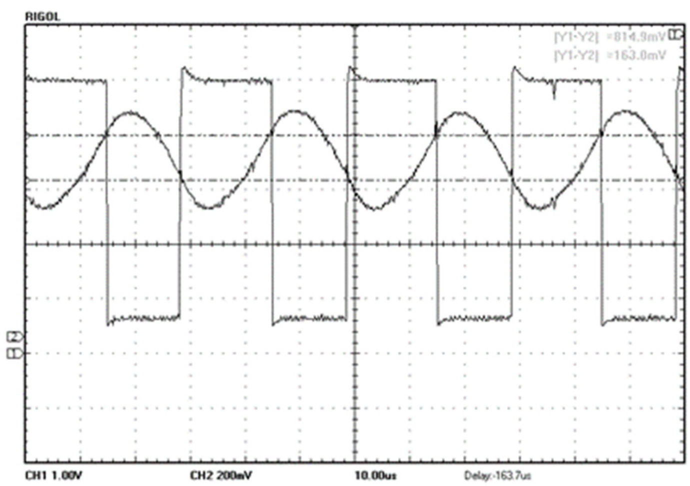

Figure 1.84: inductor current and PWM generation using PI & HSC.

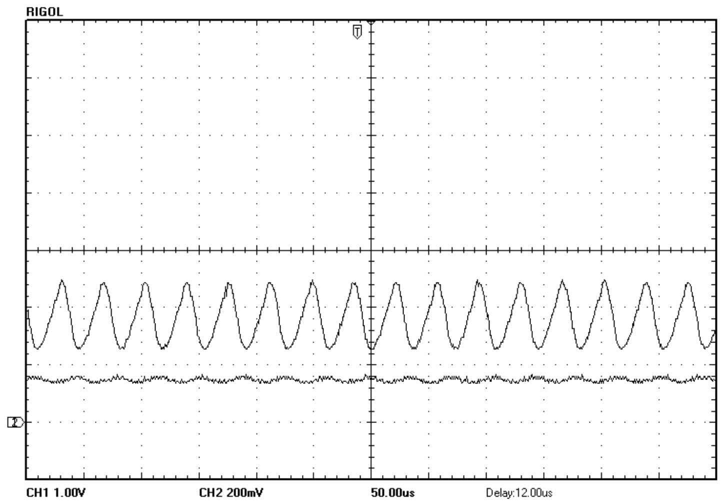

Figure 1.85: Inductor and battery charging current at CCM with 60% duty cycle.

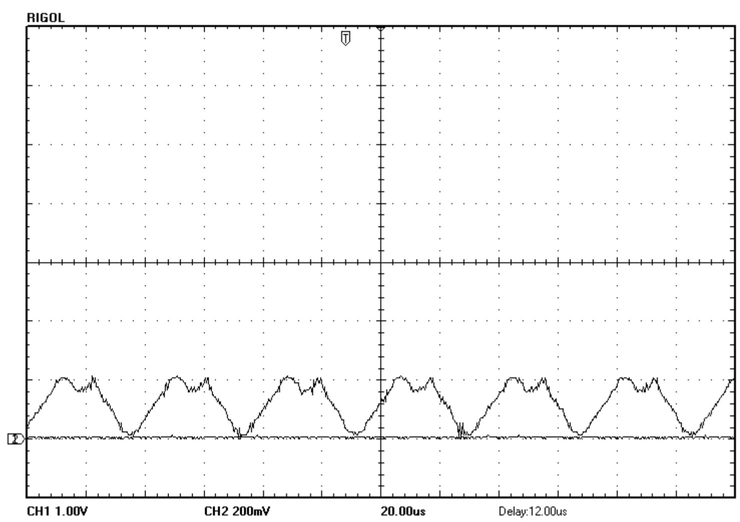

Figure 1.86: Inductor current at CVM with 45% duty cycle.

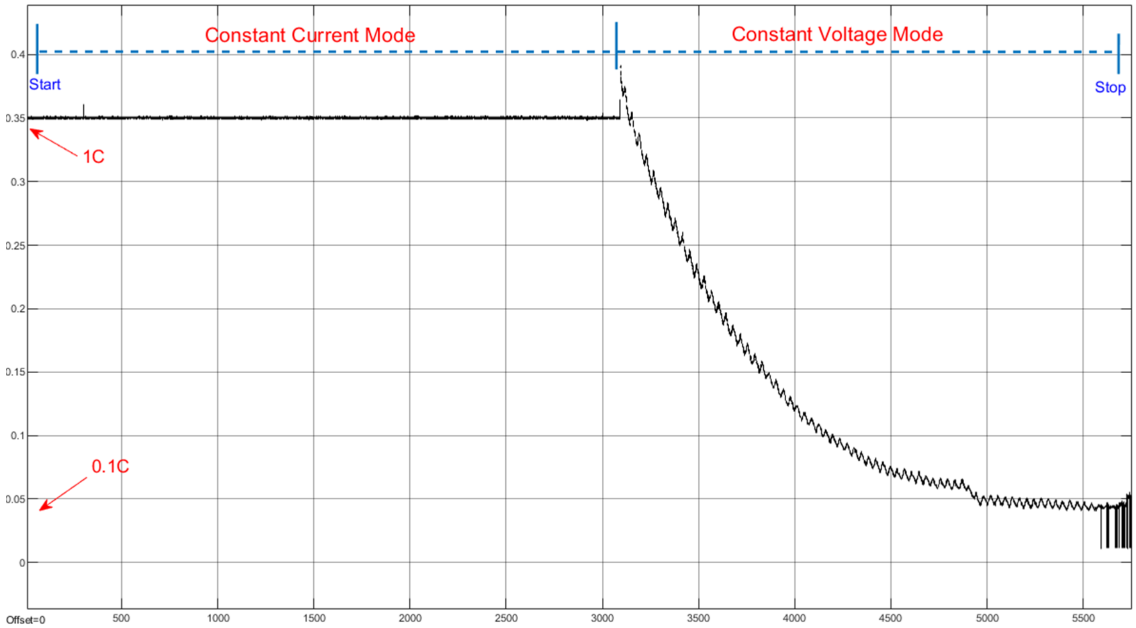

Figure 1.87: The battery charging current profile using CC/CV algorithm & FLC.

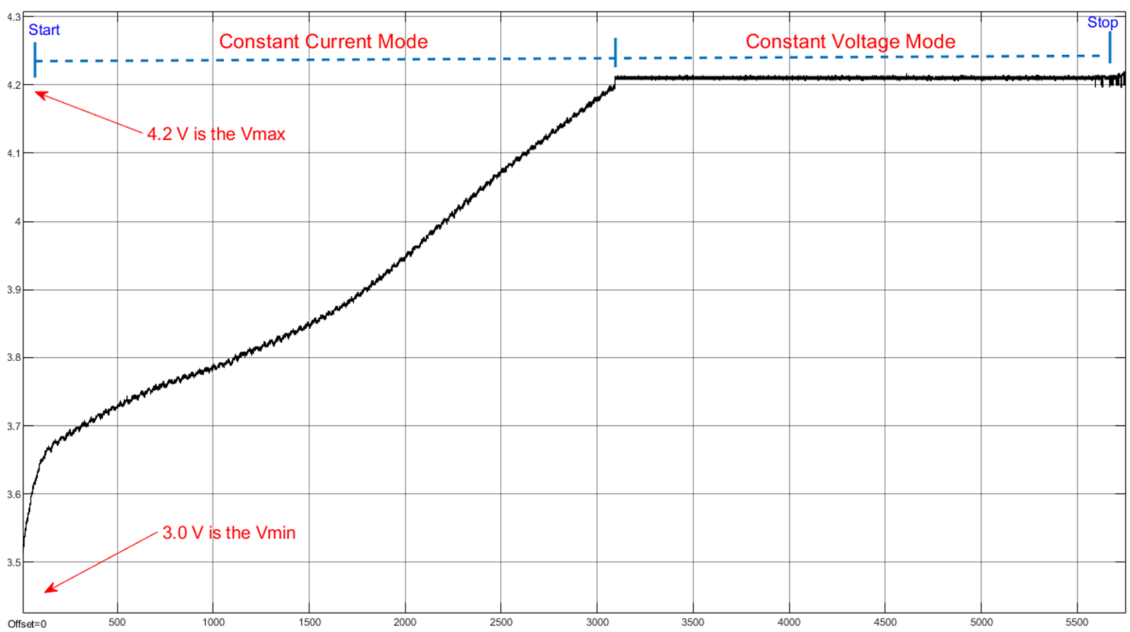

Figure 1.88: The battery charging voltage profile using CC/CV algorithm & FLC.

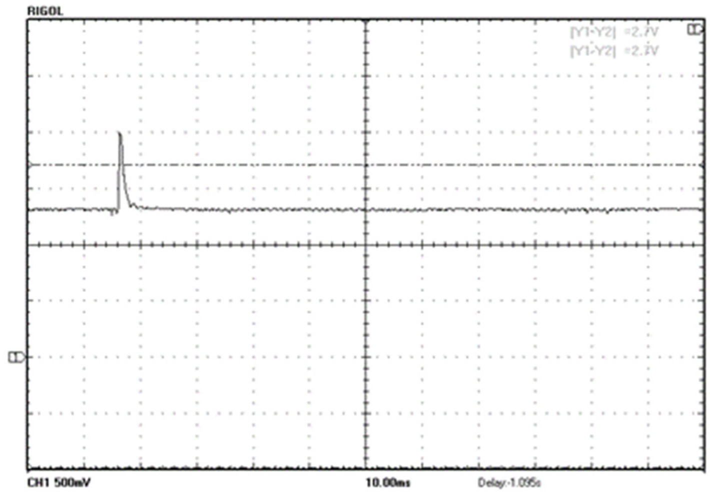

Figure 1.89: Step response of the buck converter at CCM when the load changes from 10-5 ohm using PI & HSC.

2 Conclusion and Future work

In conclusion, Multi-Source renewable energy harvesting for low power applications is possible with robust control and power management. However, the design steps show more complexity regarding DC-DC converters and sensing circuits. The solar energy is harvested using a small module that is efficient at low irradiances as the experimental results reveal where it provides alone enough power to supply the load and charge a battery. A multiple control technique was used to stabilize the MPP tracking, such as linear and non-linear controllers. The experimental results show that the non-linear controllers perform a safer response on the system. The system efficiency with respect to the expected MPP using PI, HSC, and FLC are demonstrated in table 1.11. The efficiency is calculated using Eq. 1.54 which is adding the efficiencies at different conditions using each controller, then take the ratio from the expected results. While the error calculated using Eq. 1.55 and it is used for the response time only.

$$\zeta\% = \frac{\sum Experimental\,Values}{\sum Expected\,Values} * 100\% \tag{1.54}$$

$$Error\% = \sum \frac{Experimental - Expected}{Expected} * 100\% \tag{1.55}$$

TABLE 1.11: EFFICIENCIES CALCULATION.

Controller Type	Efficiency with respect to MPP	Error of the response time
PI	97.49%	37.5%
HSC	98.65%	16.5%
FLC	95.26%	4.38%

From Table 1.11, the incremental conductance MPPT technique has a slightly low efficiency, which is the main driving controller in the harvester that forces the Linear or the non-linear controller to follow its responses. However, the INC MPPT performs differently with the controllers used in this project, as the experimental results and efficiencies calculation proves. The FLC has the lowest error percentage which mean the fastest response and the lowest MPPT efficiency. In contrast, the HSC has the best efficiency and acceptable error percentage.

Therefore, FLC show better charging efficiency compared to tracking algorithm. Nonetheless, if the fuzzy used as MPPT tracking by itself it performs better than this type of control methodology due to the dependence on the incremental conductance algorithm. In addition, the transient responses do not reflect the controller's actual response since the response of the system when a sudden change in the irradiance occurs will be driven by the MPPT algorithm. However, the nonlinear methods perform nonlinearly to adapt the changes compared to the PI controller since a rapid change in the reference value results in higher oscillations and instabilities. The error percentage shows how much the time response error between the design phase theoretically and the experimental results which many factors affects this such as the ADC clock frequency and non-linearities of the system.

The FLC battery charging is designed to charge the battery to 95% and discharge it until it reaches 50% if there is no power available, while HSC could charge the battery until 85%. Therefore, the experimental results show a very smooth charging and discharging with a capacity that lasts multiple days without recharging the battery. Finally, the error percentage is calculated to distinguish between the simulation and experimental results accuracy.

For Future work, the project still needs further data collection regarding wind energy and vibration extraction at MPP. Thus, the board needs to be modified in terms of adding the circuit for the vibration energy harvester. The bidirectional circuit is also critical for charging at CC/CV modes, and it must be added with the next board version. Finally, a better component selection is recommended to reduce the losses, which leads to an increase in the converters' efficiency. Moreover, the size of the board can be minimized to less than half of the current size to fit the wireless sensors applications.

Appendix A

Table A.1 shows the component selection (BOM) for the multi-source energy harvester. While table A.2 shows the component selection for the analog implementation of the Hysteresis switching controller (HSC).

Table A.1: BOM for the multi-source energy harvester.

Manufacturer Part #	Manufacturer	Digi-Key Part #	Customer Reference	Description
PJ-202A	CUI Devices	CP-202A-ND	J1	CONN PWR JACK 2X5.5MM KINKED PIN
AC0603KRX7R7BB103	Yageo	311-3105-1-ND	C40, C43	CAP CER 10000PF 16V X7R 0603
CC0603KRX7R7BB104	Yageo	311-1088-1-ND	C1-3,7,9,12,14-17,21,23,26,30-34,37,42,45-47	CAP CER 0.1UF 16V X7R 0603
CC1210KKX7R7BB106	Yageo	311-2027-1-ND	C4, C5, C11, C18, C19, C25, C28	CAP CER 10UF 16V X7R 1210
CC0603KRX7R7BB102	Yageo	311-4063-1-ND	C35,36,38,39,41	CAP CER 1000PF 16V X7R 0603
EMK325ABJ107MM-P	Taiyo Yuden	587-5426-1-ND	C10, C24, C29	CAP CER 100UF 16V X5R 1210
CC0603KRX7R7BB105	Yageo	311-1446-1-ND	C6, C20	CAP CER 1UF 16V X7R 0603
CR0603-JW-102ELF	Bourns Inc.	CR0603-JW-102ELFCT-ND	R26-29	RES SMD 1K OHM 5% 1/10W 0603
CR0603-FX-1002ELF	Bourns Inc.	CR0603-FX-1002ELFCT-ND	R1,6,14	RES SMD 10K OHM 1% 1/10W 0603
CR0603-FX-1503ELF	Bourns Inc.	118-CR0603-FX-1503ELFCT-ND	R3,4,5,10,11	RES SMD 150K OHM 1% 1/10W 0603
CR0603-FX-2492ELF	Bourns Inc.	CR0603-FX-2492ELFCT-ND	R2,7,9,13,15	RES SMD 24.9K OHM 1% 1/10W 0603
CR0603-FX-3602ELF	Bourns Inc.	CR0603-FX-3602ELFCT-ND	R8,12	RES SMD 36K OHM 1% 1/10W 0603
CR0603-FX-51R0ELF	Bourns Inc.	118-CR0603-FX-51R0ELFCT-ND	R30-34	RES SMD 51 OHM 1% 1/10W 0603
CR0603-FX-3300ELF	Bourns Inc.	CR0603-FX-3300ELFCT-ND	R21-25, R35-38	RES SMD 330 OHM 1% 1/10W 0603
RL2512FK-070R068L	Yageo	311-0.068TCT-ND	R_S1, R_S2, R_S3, R_S4, R_S5	RES 0.068 OHM 1% 1W 2512
OPA4340UA/2K5	Texas Instruments	296-26286-1-ND	OPA1, OPA2	IC OPAMP GP 4 CIRCUIT 14SOIC
INA138NA/3K	Texas Instruments	296-17936-1-ND	IC1, IC2, IC3, IC4, IC5	IC CURRENT MONITOR 0.5% SOT23-5
IRFZ14SPBF	Vishay Siliconix	IRFZ14SPBF-ND	Q1, Q2, Q3, Q4, Q5	MOSFET N-CH 60V 10A D2PAK
1N5819HW-7-F	Diodes Incorporated	1N5819HW-FDICT-ND	D1, D2, D3, D4	DIODE SCHOTTKY 40V 1A SOD123
US1D-13-F	Diodes Incorporated	US1D-FDICT-ND	CR1, CR2, CR3	DIODE GEN PURP 200V 1A SMA
B82477R4105M100	TDK Electronics Inc.	495-75405-6-ND	L1, L2, L3	FIXED IND 1MH 650MA 1.35 OHM SMD
IR2110STRPBF	Infineon Technologies	IR2110SPBFCT-ND	G_D1, G_D2, G_D3	IC GATE DRVR HALF-BRIDGE 16SOIC
LM324NSR	Texas Instruments	296-26097-1-ND	LM1, LM2	IC OPAMP GP 4 CIRCUIT 14SOP
BC846BLT3G	ON Semiconductor	BC846BLT3GOSCT-ND	U$5, U$6	TRANS NPN 65V 0.1A SOT-23
282837-2	TE Connectivity AMP Connectors	A113320-ND	J2, J4	TERM BLK 2P SIDE ENT 5.08MM PCB
S2B-PH-K-S(LF)(SN)	JST Sales America Inc.	455-1719-ND	J3	CONN HEADER R/A 2POS 2MM
215297-8	TE Connectivity AMP Connectors	A106654-ND	CONN_1, CONN_2	CONN RCPT 8POS 0.1 GOLD PCB
8516-4500PL	3M	MSPV16-ND	CONN_3	CONN RCPT 16POS 0.1 GOLD PCB
SQ3419AEEV-T1_GE3	Vishay Siliconix	SQ3419AEEV-T1_GE3CT-ND	U$1, U$4	MOSFET P-CHANNEL 40V 6.9A 6TSOP
60900213421	Würth Elektronik	732-2678-ND	BUS_Jumper_Female	JUMPER W/TEST PNT 1X2PINS 2.54MM
SML-310VTT86	Rohm Semiconductor	511-1301-1-ND	LED1, LED 2, LED 3, LED 4	LED RED CLEAR 0603 SMD
D01-9923246	Harwin Inc.	952-2521-ND	Bus_Jumper_Male	CONN SIL HDR MALE PIN 32POS TIN
CR0603-JW-100ELF	Bourns Inc.	118-CR0603-JW-100ELFCT-ND	R16-20	RES SMD 10 OHM 5% 1/10W 0603
T520D107M010ATE018	KEMET	399-9778-1-ND	U$8	CAP TANT POLY 100UF 10V 2917

Table A.2: BOM for the HSC analog implementation.

Manufacturer Part #	Manufacturer	Digi-Key Part #	Customer Reference	Description
LM311DR	Texas Instruments	296-1388-1-ND	U$1, U$3, U$4, U$6	IC DIFF COMP STROBE 8-SOIC
LMV834MTX/NOPB	Texas Instruments	296-35351-1-ND	U$2, U$5	IC OPAMP GP 4 CIRCUIT 14TSSOP
CD74HCT73M	Texas Instruments	296-9298-5-ND	U1	IC FF JK TYPE DUAL 1BIT 14SOIC
ERJ-PB6B1002V	Panasonic Electronic Components	P20708CT-ND	R17, R18, R19, R20, R21, R22, R23, R24	RES SMD 10K OHM 0.1% 1/4W 0805
ERA-6AEB4992V	Panasonic Electronic Components	P49.9KDACT-ND	R10, R11, R15, R16	RES 49.9K OHM 0.1% 1/8W 0805
RNCP0805FTD1K00	Stackpole Electronics Inc	RNCP0805FTD1K00CT-ND	R2, R3, R13, R14	RES 1K OHM 1% 1/4W 0805
AC1206FR-07499RL	Yageo	YAG5408CT-ND	R1, R7, R9, R12	RES SMD 499 OHM 1% 1/4W 1206
RMCF1206FT2K00	Stackpole Electronics Inc	RMCF1206FT2K00CT-ND	R4, R5, R6, R8	RES 2K OHM 1% 1/4W 1206
16TKV470M8X10.5	Rubycon	1189-2067-1-ND	C20, C21	CAP ALUM 470UF 20% 16V SMD
500R15N100JV4T	Johanson Dielectrics Inc.	709-1168-1-ND		CAP CER 10PF 50V C0G/NP0 0805
500R15N102JV4T	Johanson Dielectrics Inc.	709-1180-1-ND		CAP CER 1000PF 50V C0G/NP0 0805
160R15W104KV4T	Johanson Dielectrics Inc.	709-1183-1-ND	C2, C6, C8, C10, C13, C14, C15, C16, C17, C18-19	CAP CER 0.1UF 16V X7R 0805
C2012X7R1H105K125AE	TDK Corporation	445-8890-1-ND		CAP CER 1UF 50V X7R 0805
CL21B103KAANNNC	Samsung Electro-Mechanics	1276-2434-1-ND	C1, C9, C11, C12	CAP CER 10000PF 25V X7R 0805
CDBA140LL-HF	Comchip Technology	641-1987-1-ND		DIODE SCHOTTKY 40V 1A DO214AC
60900213421	Würth Elektronik	732-2678-ND		JUMPER W/TEST PNT 1X2PINS 2.54MM
INA138NA/3K	Texas Instruments	296-17936-1-ND	current sensor	IC CURRENT MONITOR 0.5% SOT23-5
SN74LVC2G08DCUT	Texas Instruments	296-26615-1-ND	U2	IC GATE AND 2CH 2-INP US8
215299-6	TE Connectivity AMP Connectors	A121761-ND	SV1, SV2, SV3	CONN RCPT 6POS 0.1 GOLD PCB
215297-2	TE Connectivity AMP Connectors	A106649-ND	J1, J2	CONN RCPT 2POS 0.1 GOLD PCB

Appendix B

The code used to calculate the transfer function and plot the bode plot is:

```
% Transfer Function & Bode Plot
Vs=6.5;
L=120e-6;
C=111e-6;
R=10;
num = [Vs/(L*C)]
dun= [1 1/(R*C) 1/(L*C)]
Tf= tf(num,dun)
figure (1)
step(H); grid
figure (2)
bode(Tf); grid
sisotool(Tf)
```

The code used to calculate the Ki, and Kp for PI controller design

```
% Ki, Kp calculation for frequencies around the crossover frequency
b1=0;
bo=4.88e08;
a1=900.9;
a2=1;
ao=7.508e07;
phi=75;
w=0:1:(2.56*pi);

Kp=(-a2*b1*sin(phi*w.^3)+(-a2*bo+a1*b1)*cos(phi*w.^2)+(-
a1*bo+ao*b1)*sin(phi*w)+ao*bo*cos(phi))/(((b1^2)*w.^2+bo^2));
Ki= w.*(-a2*b1*cos(phi*w.^3)+(a2*bo-a1*b1)*sin(phi*w.^2)+(ao*b1-
a1*bo)*cos(phi*w)-ao*bo*sin(phi))/(((b1^2)*w.^2+bo^2));

plot (ki,kp); grid
xlim([-0.02 0.2])
xlabel("Kp")
ylabel("Ki")
title("Stability Boundry Locus")
```

The Incremental Conductance MATLAB code:

```
function D_PO = PandO(V,I,DD, Act)
% # codegen
% ****************************************************************
% MATLAB implementation of a Incremental Conductance algorithm
% for Maximum Power Point Tracking. This algorithm is designed
% to operate with a buck converter
%
% Created by Carlos Osorio
% Modified by Maen Marji
%****************************************************************
%
% Define internal values for the voltage and power as persistent
% Variables

persistent Vold Iold Pold Dold Dmin Dmax

% Initialize the internal values for the voltage and power on the
% first pass

if isempty(Vold)
    Vold = 0;
    Iold = 0;
    Pold = 0;
    Dold = 0.5;
    Dmin = 0.01;
    Dmax = 1;
end
% Initialize algorithm parameters
deltaD=DD;
```

```
D_PO=Dold;
% Calculate measured array power
P = V*I;
dV= V-Vold;
dI= I-Iold;
Slope= dI/dV;
dP=P-Pold;
% Increase or decrease duty cycle based on conditions
if Act == 1
    if dV == 0
        if dI == 0
        %D_PO = Dold;
        else
            if (dI) > 0
               D_PO = Dold + deltaD;
            end
            if (dI) < 0
        D_PO = Dold - deltaD;
            end
        end
   else
   if Slope == -(I/V)
    %D_PO = Dold;
   else
       if Slope > -(I/V)
        D_PO = Dold - deltaD;
       end
       if Slope < -(I/V)
        D_PO = Dold + deltaD;
       end
   end
    end
else
  D_PO=Dold;
end

if D_PO >= Dmax | D_PO<= Dmin
    D_PO=Dold;
end
Iold=I;
Dold=D_PO;
Vold=V;
Pold=P;
end
```

Appendix C

The Overall experimental setup is shown below:

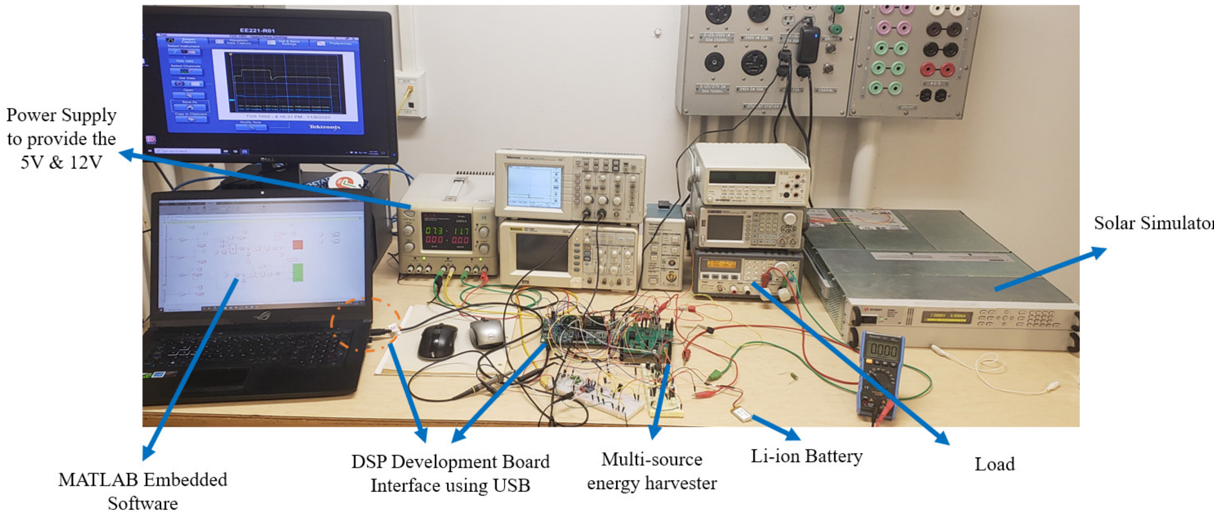

Figure C.1: The experimental setup.

References:

[1] P. Huang, W. Xiao, J. C. -. Peng and J. L. Kirtley, "Comprehensive Parameterization of Solar Cell: Improved Accuracy with Simulation Efficiency," in *IEEE Transactions on Industrial Electronics*, vol. 63, no. 3, pp. 1549-1560, March 2016, doi: 10.1109/TIE.2015.2498139.

[2] Beeby, Stephen, and Neil White. *Energy Harvesting For Autonomous Systems*, Artech House, 2010. *ProQuest Ebook Central*, https://ebookcentral.proquest.com/lib/csufresno/detail.action?docID=946528.

[3] https://re.emsd.gov.hk/english/solar/solar_ph/Electrical_Properties_of_PV_Modules.html

[4] Mohammed S, Sheik & Devaraj, D.. (2015). Fuzzy based maximum power point tracking controller for stand alone photovoltaic system using MATLAB/Simulink. International Journal of Applied Engineering Research. 10. 3101-3106.

[5] T. Kanda, L. P. Mdakane, C. J. J. Labuschagne and M. J. Kamper, "Dynamics of Maximum Power Point Wind Energy Battery Charging Systems," *2019 Southern African Universities Power Engineering Conference/Robotics and Mechatronics/Pattern Recognition Association of South Africa (SAUPEC/RobMech/PRASA)*, Bloemfontein, South Africa, 2019, pp. 576-581. doi: 10.1109/RoboMech.2019.8704824

[6] J Smith and M Hadingham, HatchGoba, Africa "Integrating a wind farm into a transmission or distribution system" 2014 at eepuplisher https://www.ee.co.za/article/integrating-wind-farm-transmission-distribution-system.html.

[7] Asis Sarkar*, Dhiren Kumar Behera, "Wind Turbine Blade Efficiency and Power Calculation with Electrical Analogy, " International Journal of Scientific and Research Publications, Volume 2, Issue 2, February 2012 1 ISSN 2250-3153Y.

[8] S. Kumari, V. Kushwaha and T. N. Gupta, "A Maximum Power Point Tracking For a PMSG Based Variable Speed Wind Energy Conversion System," *2018 International Conference on Power Energy, Environment and Intelligent Control (PEEIC)*, Greater Noida, India, 2018, pp. 789-794, doi: 10.1109/PEEIC.2018.8665484.

[9] Garimella, Raghu Chandra & Vedala, Rama Sastry & Mohiuddin, Mohammed. (2015). Piezo-Gen - An Approach to Generate Electricity from Vibrations. Procedia Earth and Planetary Science. 11. 445-456. 10.1016/j.proeps.2015.06.044.

[10] Yang, Zhengbao & Zhou, Shengxi & Zu, Jean & Inman, Daniel. (2018). High-Performance Piezoelectric Energy Harvesters and Their Applications. Joule. 2. 642-697. 10.1016/j.joule.2018.03.011.

[11] Murata Manufacturing Co at
https://www.murata.com/en-us/products/timingdevice/ceralock/basic/description

[12] Mouapi, A.; Hakem, N. Electrical Optimization of Piezoelectric Energy Harvesting System in Vehicles. In Proceedings of the International Conference on Energy, Environment and Economics, Edinburgh, UK, 16–18 August 2016.

[13] DC1459B-A. Available online: http://www.analog.com/en/design-center/evaluation-hardware-and-software/ evaluation-boards-kits/dc1459b-a.html#eb-overview (accessed on 30 April 2020).

[14] Circuit Digest at https://circuitdigest.com/microcontroller-projects/programming-attiny13-with-arduino-uno-control-a-servo-motor

[15] Brigitte Hauke, Texas instrument application report " Basic Calculation of a Buck Converter's Power Stage" SLVA477B–December 2011–Revised August 2015 at
https://www.ti.com/lit/an/slva477b/slva477b.pdf?ts=1604973949947&ref_url=https%253A%252F%252Fwww.google.com%252F

[16] Brigitte Hauke, Texas instrument application report " Basic Calculation of a Boost Converter's Power Stage" SLVA372C–November 2009–Revised January 2014 at

https://www.ti.com/lit/an/slva372c/slva372c.pdf?ts=1605123202534&ref_url=https%253A%252F%252Fwww.google.com%252F

[17] Hagedorn, Julian, "Application Report Basic Calculations of a 4 Switch Buck-Boost Power Stage" *Texas Instrument SLVA535B*–January 2018–Revised July 2018 at https://www.ti.com/lit/an/slva535b/slva535b.pdf?ts=1605050281766&ref_url=https%253A%252F%252Fwww.google.com%252F

[18] A. Koran, K. Sano, R. Kim and J. Lai, "Design of a photovoltaic simulator with a novel reference signal generator and two-stage LC output filter," *2009 IEEE Energy Conversion Congress and Exposition*, San Jose, CA, 2009, pp. 319-326, doi: 10.1109/ECCE.2009.5316190.

[19] L. Arun Shravan and D. Ebenezer, "Maximum Power Point Tracking (MPPT) for a Solar Photovoltaic System: A Review", *Applied Mechanics and Materials*, vol. 787, pp. 227-232, 2015.

[20] Rahman, Shusmita, Nadia Sultana Oni, and Quazi Abdullah Ibn Masud. "Design Of A Charge Controller Circuit With Maximum Power Point Tracker (MPPT) For Photovoltaic System". (2012).

[21] Silberberg, M. (2006). *Chemistry: The Molecular Nature of Matter and Change*, 4th Ed. New York (NY): McGraw-Hill Education. p. 935, ISBN 0077216504.

[22] B. Wu, V. Yufit, M. Marinescu, G. J. Offer, R. F. Martinez-Botas, and N. P. Brandon, "Coupled thermal-electrochemical modelling of uneven heat generation in lithium-ion battery packs," *Journal of Power Sources*, vol. 243, pp. 544–554, 2013.

[23] J. Kim, S. Lee, and B. H. Cho, "Complementary cooperation algorithm based on DEKF combined with pattern recognition for SOC/capacity estimation and SOH prediction," *IEEE Transactions on Power Electronics*, vol. 27, no. 1, pp. 436–451, 2012.

[24] Shen, Weixiang & Vo, Thanh & Kapoor, Ajay. (2012). Charging algorithms of lithium-ion batteries: An overview. Proceedings of the 2012 7th IEEE Conference on Industrial Electronics and Applications, ICIEA 2012. 1567-1572. 10.1109/ICIEA.2012.6360973.

[25] "A Designer's Guide to Lithium Battery Charging." *Digi-Key Electronics*. Steven Keeping, 25 Sept. 2012. Web. at http://www.digikey.com/en/articles/techzone/2012/sep/a-designers-guide-to-lithium-battery-charging

[26] Hart, Daniel W. Power electronics / Daniel W. Hart. p. cm. 2011. Includes bibliographical references and index. ISBN 978-0-07-338067-4 (alk. paper) TK7881.15.H373 2010 621.31'7—dc22.

[27] *Ruye Wang 2003-10-17* "The Bode plot of second order system" at http://fourier.eng.hmc.edu/e101/lectures/Bode/node8

[28] M. M. Garg, Y. V. Hote, M. K. Pathak and L. Behera, "An Approach for Buck Converter PI Controller Design Using Stability Boundary Locus," *2018 IEEE/PES Transmission and Distribution Conference and Exposition (T&D)*, Denver, CO, 2018, pp. 1-5, doi: 10.1109/TDC.2018.8440291.

[29] K. Swathy, S. Jantre, Y. Jadhav, S. M. Labde and P. Kadam, "Design and Hardware Implementation of Closed Loop Buck Converter Using Fuzzy Logic Controller," *2018 Second International Conference on Electronics, Communication and Aerospace Technology (ICECA)*, Coimbatore, 2018, pp. 175-180, doi: 10.1109/ICECA.2018.8474570.

[30] L. Fraas, and L. Patain, " Solar cells and their applications". Hoboken, New Jersey: Wiley, 2010, pp. 77.

[31] A. H. Dida and M. Bekhti, "Study, modeling and simulation of the electrical characteristic of space satellite solar cells," *2017 IEEE 6th International Conference on Renewable Energy Research and Applications (ICRERA)*, San Diego, CA, 2017, pp. 983-987. doi: 10.1109/ICRERA.2017.8191205K. Elissa, "Title of paper if known," unpublished.

[32] Anas El Filali, El Mehdi Laadissi and Malika Zazi, "Modeling and simulation of photovoltaic system employing perturb and observe mppt algorithm and fuzzy logic control"31st July 2016. Vol.89. No.2 © 2005 - 2016 JATIT & LLS; SSN: 1992-8645

[33] Dr. Nagy Bengiamin " Lecture 6 Fuzzy Logic Control for ECE 230 Non-linear Control". ECE department, CSU, Fresno. Spring 2020.

[34] INA138 Datasheet Texas Instrument "INA1x8 High-Side Measurement Current Shunt Monitor" SBOS122E – DECEMBER 1999–REVISED DECEMBER 2017.

[35] International Rectifier IR2110 Datasheet "IR2110(S)PbF/IR2113(S)PbF HIGH AND LOW SIDE DRIVER ". Data Sheet No. PD60147 rev.V June 3rd 2019.

[36] PSIM Inc. "DSP Development Board User's Manual Version 12". February 2019.

[37] T. Kim, H. Lee and S. Kwak, "Open-Circuit Switch-Fault Tolerant Control of a Modified Boost DC–DC Converter for Alternative Energy Systems," in *IEEE Access*, vol. 7, pp. 69535-69544, 2019, doi: 10.1109/ACCESS.2019.2919238.

[38] https://www.samlexsolar.com/learning-center/solar-cell-module-array.aspx

[39] https://www.allaboutcircuits.com/technical-articles/analysis-of-four-dc-dc-converters-in-equilibrium

[40] Marwan Rosyadi, S. M. Muyeen, Rion Takahashi, and Junji Tamura "A Design Fuzzy Logic Controller for a Permanent Magnet Wind Generator to Enhance the Dynamic Stability of Wind Farms" MDPI Journal, 22 November 2012 at: https://www.mdpi.com/2076-3417/2/4/780/htm

[41] Dr. Nagy Bengiamin " Lecture 4, Phase Plane Analysis ". ECE department, CSU, Fresno. Spring 2020.

[42] Dr. Nagy Bengiamin " Lecture 1, Introduction to ECE 230 ". ECE department, CSU, Fresno. Spring 2020.

[43] A. Koran, K. Sano, R. Kim and J. Lai, "Design of a photovoltaic simulator with a novel reference signal generator and two-stage LC output filter," *2009 IEEE Energy Conversion Congress and Exposition*, San Jose, CA, 2009, pp. 319-326, doi: 10.1109/ECCE.2009.5316190.

[44] https://www.oreilly.com/library/view/high-performance-control/9781119942108/c02anchor-2.html

[45] Sridhar, Harshid & ks, Meera. (2014). Study of grid connected solar photovoltaic system using real time digital simulator. 10.1109/ICAECC.2014.7002473.

[46] L. Cai and R. E. White, *Journal of Power Sources*, **196**, 5985 (2011).

[47] Y. Xie, J. Kim, M. Lee, J. Park and W. Na,“ An Impedance Behavior Study of Commercial NCA Cylindrical Battery Cells at Different SOCs,” published in the Journal of The Electrochemical Society, 2021, 168, 090548